Journal of Applied Fluid Mechanics, Vol. 18, No. 5, pp. 1266-1284, 2025.
Available online at www.jafmonline.net, ISSN 1735-3572, EISSN 1735-3645.
https://doi.org/10.47176/jafm.18.5.3094

Hydrodynamic and Thermodynamic Behavior of Liquid Methane in a Vertical Feed Pipe

K. Raj and P. R. L. Raj†

Department of Aerospace Engineering and Applied Mechanics, Indian Institute of Engineering Science & Technology, Shibpur, Howrah 711103, India

†*Corresponding Author Email: plraj@aero.iiests.ac.in*

ABSTRACT

During the chill-down procedure for a space application system, a multiphase flow of extremely cold propellants will undoubtedly occur in the feed lines. Due to flow instability and varying cooling rates, this cooling technique produces dynamic changes that are challenging to control. Over the past few decades, research has extensively examined the multiphase behaviour of various cryogens, such as liquid nitrogen, liquid hydrogen, and liquid oxygen, while few studies focus on liquid methane. This study addresses this gap by investigating the hydrodynamic and thermodynamic characteristics of LCH_4-VCH_4 multiphase flow in a vertical cryogenic pipe using a well-validated, three-dimensional Volume of Fluid (VOF) model. Further, the current study employs an Eulerian flow scheme coupled with an energy equation to accurately capture the multiphase flow dynamics of liquid methane across various inlet velocities and temperatures. The volume fractions are used to investigate the flow pattern, and the interaction between the two phases and the two-phase flow structure is investigated using velocity profiles and phase distribution. Further, the bulk mean and near-wall temperature results were analysed to understand the temperature variation inside the pipe. Increased inlet temperatures at constant velocities enhance vapour volume fractions, while higher velocities reduce vapour generation, leading to decreased bulk mean temperature due to reduced heat transfer. However, a significant rise in vapour flow rates occurs at elevated temperatures with constant velocity. The volume fraction results show the formation of bubble, annular, and slug flow patterns in the flow regime.

Article History

Received September 5, 2024
Revised November 23, 2024
Accepted December 22, 2024
Available online March 4, 2025

Keywords:

Multiphase flow
VOF
Heat transfer
Cryogenics
Flow identification

1. INTRODUCTION

The space industry has seen a growing push to establish more affordable, commercially oriented access to space, with a substantial drop in the cost per kilogram of cargo to orbit already achieved. This has been made partially feasible by deliberate complexity reductions and improvements in launch vehicle reusability (Jones, 2018; Heldens et al., 2021). Liquid rocket engines are widely used in reusable launch vehicles due to their high specific impulse (Meyer et al., 2012). The liquid propellant used for upcoming deep space missions is being tested by several businesses for use in reusable launch vehicles (Baiocco & Bonnal, 2016; Iannetti et al., 2017). Due to the vast distance between Earth and Mars, human missions to Mars are the most difficult. A high specific impulse is required to quickly traverse the vast distance between Earth and Mars. It would be highly advantageous if the propellant could be derived chemically from Mars's atmosphere for the return missions (Salerno & Kittel, 1999; Rapp, 2016).

Methane is considered an adequate substitute for liquid propellant for rocket propulsion applications, which has raised interest in developing liquid oxygen (LOX)/methane (CH_4) rocket engines. This curiosity is due to the distinct characteristics of the cryogenic-propellant methane compared to other conventional liquid propellants in rocket engine applications. Methane has the edge over cryogenic hydrogen due to its lower storage requirements, greater density, and higher vaporisation temperature. It also has a higher specific impulse, larger coking limit and a better cooling capacity than kerosene (Burkhardt et al., 2004). Moreover, methane might be extracted from the surface of Mars or other planets in space and used as fuel with the process known as in-situ resource utilisation (ISRU) (Yung et al., 2018).

Nomenclature

Symbols

ρ	density	r_l	relaxation time for liquid
ρ_l	liquid density	r_v	relaxation time for vapor
ρ_v	vapor density	P	pressure
ρ_w	metal wall density	g	gravity
α_l	liquid fraction	F_{CSF}	continuum surface force
α_v	vapor fraction	σ_{lv}	surface tension coefficient
μ	dynamic viscosity	C_v	curvature correction coefficients for vapor
μ_l	liquid dynamic viscosity	e	energy
μ_v	vapor dynamic viscosity	e_l	liquid energy
t	time	e_v	vapor energy
$\dot{m}_{lv}$	mass evaporated	k	conductivity
$\dot{m}_{vl}$	mass condensed	k_l	liquid conductivity
$\vec{u}_v$	vapor phase velocity	k_v	vapor conductivity
$\vec{u}$	velocity vector	S_E	energy source term
$\vec{u}_{in}$	inlet velocity	$C_{p,l}$	liquid specific heat capacity
T	temperature	$C_{p,v}$	vapor specific heat capacity
T_b	bulk mean temperature	C_w	metal wall specific heat capacity
T_l	liquid temperature		
T_{wall}	wall temperature		
T_{SAT}	saturation temperature		
T_{in}	inlet temperature		

Abbreviation

VOF	Volume Of Fluid
CFD	Computational Fluid Dynamics
LCH_4	Liquid Methane
VCH_4	Vapor Methane

The multiphase phenomenon occurs in the liquid rocket in many regions where the cryogenic fluid is used at low temperatures. In cryogenic liquid storage tanks, liquid cryogenic is stored below its boiling temperature; thus, a phase change occurs due to Boil-off-Gas (BOG) (Ferrín & Pérez-Pérez, 2020; Jeon et al., 2021; Al Ghafri et al., 2022). The other area is where the cryogenic propellants are transferred from the storage tank to the engine through feed pipes in aerospace applications, where the chill-down procedure is utilised heavily for an ensuing single-phase flow to prevent combustion instability upon restart (Hartwig et al., 2015). It is worth mentioning that multiphase occurs in numerous thermohydraulic systems, including evaporators, chemical reactors, oil pipelines, and nuclear reactors (Jouhara et al., 2023; Gao et al., 2024).

Multiphase phenomena have been studied throughout the past few decades, and researchers have gained more attraction toward experimental studies due to advancements in instruments, sensors, and image-processing devices (Xie et al., 2017; Ling et al., 2021; Sun et al., 2023; Zeghloul & Al-Sarkhi, 2023; Sha et al., 2024; Zhang et al., 2024). Fang et al. (2016) examined the liquid nitrogen boiling in a vertical conduit transferred by varying the pressure, heat flux, and mass flow. It was reported that upward flow nitrogen boiling exhibits a V-shaped curve with two crucial heat flux points in a vertical macro-channel with uniform heating. The system under investigation found four distinct flow patterns: bubbly, annular, scattered, and mist flow. The heat transfer coefficient increased as the flow changed from bubbly to annular, while the dry out-type convective heat flux appeared as the flow changed from scattered to mist. Fu et al. (2008) captured the patterns of liquid nitrogen flow and bubbling in a vertical mini-tube using a high-speed camera and observed four different flow patterns: bubbly, slug, churn, and circular flow. The flow regime image was reported to have only annular flow when the vapour quality is higher than 0.15. Moreover, compared to a conventional fluid, the transition from bubbly flow to slug flow moves at higher gas speeds and churn to annular flow transition lines move at lower gas speeds.

Hartwig et al. (2015) experimentally investigated the chill-down of liquid hydrogen (LH_2) and liquid nitrogen (LN_2) by examining the temperature, heat transfer, and critical heat flux. The results indicate hydrogen has a quicker chill-down process because of its lower density, surface tension, and viscosity. Further, due to variations in parasitic heat loss, higher flow rate LH_2 tests are more successful than lower flow rate LN_2 trials. Hu et al. (2012) used a Pyrex test tube and liquid nitrogen to investigate heat transfer in a vertical pipe chill-down process. The effects of different mass flow rates on critical heat flux, rewetting temperature, and quench front movement were determined by measuring temperature variations. It was found that the crucial heat flux decreases with an increase in mass flow rate, but the rewetting temperature and quench front velocity rise. Moreover, the chill-down period is prolonged for uphill flow, whereas the critical heat flux and heat transfer coefficient are more significant for downhill flow, but the quench front movement speed is slower.

Several multiphase flows of various cryogenic fluids were investigated by computational methods in the last few decades (Chuang & Hibiki, 2015; Chen et al., 2018; Archipley et al., 2022; Zhang et al., 2022; Duan et al., 2023). Chen et al. (2020) developed a numerical model to investigate flow film boiling in the cryogenic chilldown process. The model examined how wall superheat, and inlet mass flux affect the two-phase flow structure and

Table 1 Liquid and gas phase properties of methane were used in the present simulations

	Liquid Methane	**Vapour Methane**
Density (kg/m^3)	-558.75028 + 44.06114 T -0.68466 T^2 + 0.0046 T^3 -1.165 * 10^{-5} T^4	2.6049
Kinematic viscosity (Pa-s)	0.00943 - 0.00032 T + 4.272 * 10^{-6} T^2 - 2.564 * 10^{-8} T^3 + 5.827 * 10^{-11} T^4	4.5034×10^{-6}
Specific heat capacity (J/kg K)	15523.2487 -482.2137 T + 7.122610723 T^2 - 0.046775447 T^3 + 1.1655 10^{-4} T^4	2259
Thermal conductivity (W/m K)	-3.04763 + 0.13162 T - 0.00196 T^2 + 1.294 * 10^{-5} T^3 - 3.205 * 10^{-8} T^4	0.012121
Surface tension (N/m)	0.011950	
Specific latent heat (J/kg)	515000	
Contact angle (degree)	90	
Boiling temperature (K)	116.66	

heat transfer. Most of the wall heat flux comes from vapour film and liquid layer changes at low inlet mass flow rates. It was found that most heat transfer comes from axial convection at higher inlet mass flow rates. When the wall superheat goes up, the pressure goes down, but the pressure goes down when the inlet mass flow goes up. The wall superheat affects the size of the fluctuations, while mass flow affects the main frequency of pressure drops. Agarwal & Dondapati (2020) conducted a numerical analysis of the hydrodynamic characteristics of a multiphase flow of liquid hydrogen through a cryogenic feed line at both microgravity and terrestrial gravity. With the clear observation of the annular-core interface, the vapour phase distribution confirms that creating an annular dominant slug flow regime is more prevalent in microgravity than terrestrial gravity.

Jeon et al. (2021) focus on the precise computation of Boil-off-Gas and Boil-off-Rate, essential for constructing the containment cargo system. The heat transfer process in the insulation system and the phase change of the multiphase-thermal flow in the cryogenic liquid tank are investigated using the VOF model. Further, it was found that there was a discernible rise in the cooling rate at the second stage of the cooling process. As a result, the reduction rate of the mean pressure in the compression space underwent a distinct acceleration phase. Ahammad et al. (2016) computationally analysed the film boiling of cryogenic liquid nitrogen and liquefied natural gas (LN_2 and LNG) to find the interface morphology, wall heat flux, bubble frequency, and bubble diameter. The simulations show that various cryogenic liquids exhibit different bubble formation trends based on the temperature.

The literature shows a scarcity of investigations on hydrodynamic and thermodynamics studies conducted on vertical pipe arrangements for the cryogenic propellant. Moreover, due to the low temperature of liquid methane, handling cryogenic propellant becomes quite difficult, posing challenges in conducting experiments. An inappropriate calibration of thermocouples, pressure gauges, or sensors may lead to incorrect measurements, thereby affecting the reliability of experimental data. Additionally, managing heat leakage to the ambient through the feed pipe presents a significant challenge during experiments, potentially compromising the reliability of the results. These challenges are compounded for the lack of study on the multiphase phenomena of cryogenic propellants and the effects of wall temperature (Srinivasan et al., 1974; Antar & Collins, 1995; Hu et al., 2012). It is worth mentioning that the multiphase phenomena on cryogenic methane are very limited in the previous literature. Investigating the methane liquid-gas flow dynamics and interfacial behaviour is essential to understanding multiphase phenomena and related cooling effects.

The current study focuses on building a three-dimensional computational model of a cryogenic feed line to examine the hydrodynamic and thermodynamic characteristics of two-phase cryogenic flows. For this purpose, a conjugate heat transfer computational model is developed based on the VOF model to account for the multiphase phenomenon. After the validation of computational models, the computational model is employed to investigate the two-phase flow patterns along the various flow regimes. The velocity profile at different locations in the flow regime and the mass flow rate of liquid and vapour phases are examined better to understand the multiphase flow hydrodynamic and thermodynamic properties. The current investigation extended the bulk mean temperature and near-wall temperature variation to get more insight into the thermodynamic properties of methane at various temperatures.

2. COMPUTATIONAL MODELLING

The present work uses a three-dimensional vertical feed pipe to investigate liquid methane's multiphase flow and heat transfer characteristics. The liquid methane (LCH_4) is fed vertically inside the pipe through the inlet of the pipe with an adiabatically insulated wall with a 50 mm diameter (d) and 1 m length (l), as shown in Fig. 1(a). The wall of the pipe is maintained at a constant temperature (27 ^{0}C), which is assumed to be the surrounding temperature of the feed pipe and pressure at the inlet of the pipe is maintained at 1.5 bar. The liquid and gaseous methane's physical properties have been utilised from the NIST database (Linstrom & Mallard, 2001) where the piecewise polynomial equation with respect to temperature (T) is used for liquid methane properties, as shown in Table 1.

The hydrodynamic characterisation of two-phase flow necessitates tracking the volume fraction of each

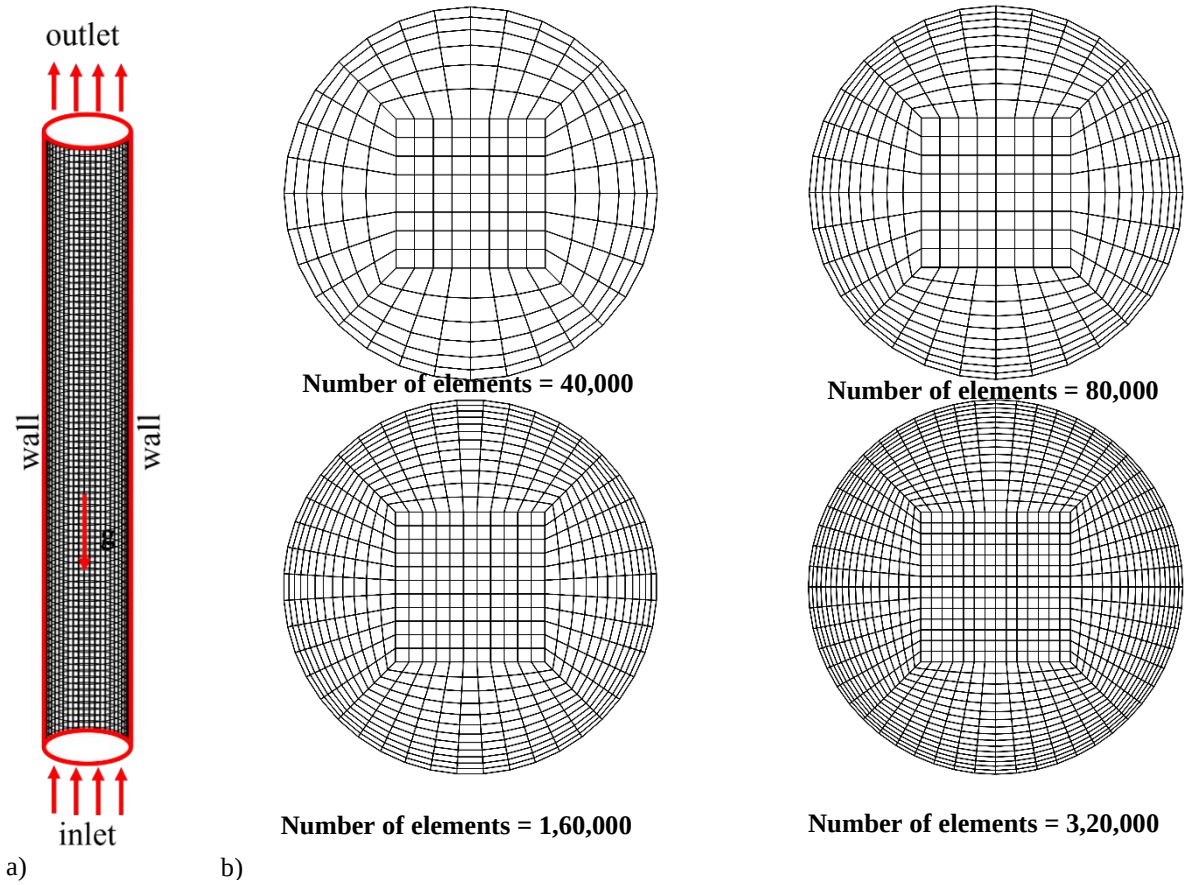

Fig. 1 Meshed geometry with boundary condition and grid independent case study a) along longitudinal direction and b) along radial direction

phase across the entire domain. Therefore, it is necessary to solve conservation equations for mass, momentum, and phase fraction in each phase, leading to an increase in the number of unknown variables that must be determined. The present study adopted a transient simplified approach to the Eulerian model, namely the volume of fluid (VOF) scheme (Abdulkadir et al., 2015; Davanipour et al., 2018). This approach employs a single set of equations based on a conservation equation of reducing complexity to describe a novel technique for the surface tracking of multiple immiscible phases. Each new phase's volume fraction is entered into the calculations, ensuring that the sum of all phase fractions within a control volume equals one. The VOF model stands out for its ability to accurately represent intricate fluid interfaces in the flow area. It provides simplicity and flexibility and is highly suitable for continuous-phase interaction issues. The tool is highly trusted for studying multiphase flow phenomena due to its mass conservation and accuracy in interface dynamics. The Navier-Stokes equations can be solved simultaneously using computational fluid dynamics (CFD) modelling. These equations considered density (ρ) and dynamic viscosity (μ), which are influenced by the volume fraction of each phase, which are calculated using equations (1) and (2) (Zheng et al., 2019; Agarwal & Dondapati, 2020).

$$\rho = \alpha_l \rho_l + (1-\alpha_l)\rho_v \tag{1}$$

$$\mu = \alpha_L \mu_L + (1-\alpha_L)\mu_V \tag{2}$$

The solver uses numerical methods to handle the two distinct phases present in the mesh grid as follows:

- If the cell consists of the liquid phase: $\alpha_l = 1$
- If the cell consists of the vapour phase: $\alpha_v = 1$
- If a cell consists of the two-phase liquid and vapour, then $0 < \alpha_l < 1$.

Continuity Equation

The evaporation–condensation mass transfer during the phase change is governed using the Lee model (Lee, 2013). The vapour transport equation (3) controls the mass transfer of liquid to vapour in this model, including evaporation and condensation. Here, $\dot{m}_{lv}$, $\dot{m}_{vl}$ represents the rate of mass transfer from liquid phase to vapour phase and from vapour phase to liquid phase due to evaporation and condensation, respectively.

$$\frac{\partial \alpha_v \rho_v}{\partial t} + \nabla \cdot (\rho_v \alpha_v \vec{u}_v) = \dot{m}_{lv} - \dot{m}_{vl} \tag{3}$$

For the evaporation-condensation problem, equations (4) and (5) are utilised to categorise positive mass transfer as occurring from the liquid to the vapour. The following

temperature zones are used to characterize the mass transfer (Fertahi et al., 2018).

If $T_l > T_{SAT}$

$$\dot{m}_{lv} = r_v \times \alpha_l \rho_l \frac{T - T_{SAT}}{T_{SAT}} \tag{4}$$

If $T < T_{SAT}$

$$\dot{m}_{vl} = r_l \times \alpha_v \rho_v \frac{T - T_{SAT}}{T_{SAT}} \tag{5}$$

The phase transition takes place under conditions of constant pressure and is influenced by the saturation temperature (T_{SAT}). The parameters r_v and r_l have been identified as crucial factors in determining mass transfer time, as noted by Liu et al. (2016). It is imperative that these parameters are carefully calibrated to ensure optimal performance. It is postulated that the source term can be obtained through the multiplication of the rate of mass transfer by the latent heat.

The volume fraction equation, which is a continuation of the equations previously provided, resolves the secondary phase. Equation (6) is used to compute the primary phase.

$$\sum_{L=1}^{n} \alpha_L = 1 \tag{6}$$

Momentum Equation

The VOF model focuses on the solution of a single equation of motion within the flow field. The calculation of velocity is distributed across the two phases. The equation for momentum, denoted as Eq. (7), is expressed as follows:

$$\frac{\partial \rho \vec{u}}{\partial t} + \nabla \cdot (\rho \vec{u}\vec{u}) = -\nabla P + \nabla \cdot \tau + \rho g + F_{CSF} \tag{7}$$

The fluid is subject to the forces of gravity, pressure, viscous friction, and surface tension. By including the term F_{CSF} in the momentum equation, the influence of the surface tension is taken into account. The continuous surface force is represented by Eq (8), which was introduced by Brackbill et al. (1992).

$$F_{CSF} = 2\sigma_{lv} \frac{\alpha_l \rho_l C_v \nabla \alpha_v + \alpha_v \rho_v C_l \nabla \alpha_l}{\rho_l + \rho_v} \tag{8}$$

Here, C represents the curvature of the surface, whereas σ_{lv} represents the coefficient of surface tension. The temperature-dependent functions for the coefficient of surface tension and the density of the liquid phase ρ_l, as described by Equations (9) and (10), were expressed using the same formula as Equation (8).

$$\sigma_{LV} = 0.09805856 - 1.845 \times 10^{-5} T - 2.3 \times 10^{-7} T^2 \tag{9}$$

$$\rho_L = 859.0083 + 1.252209 \times T - 0.0026429 T^2 \tag{10}$$

Energy Equation

The energy equation in the VOF model considers energy (e) and temperature (T) as mass averaged variables as given in Eqn. (11) and (12).

$$\frac{\partial \rho e}{\partial t} + \nabla \cdot (\rho e \vec{u}) = \nabla \cdot (k \nabla T) + \nabla \cdot (p \vec{u}) + S_E \tag{11}$$

$$e = \frac{\alpha_l \rho_L e_l + \alpha_v \rho_v e_v}{\alpha_l \rho_l + \alpha_v \rho_v} \tag{12}$$

$$e_v = C_{p,v} \left(T - T_{SAT} \right) \tag{13}$$

$$e_l = C_{p,l} \left(T - T_{SAT} \right) \tag{14}$$

The mixture's thermal conductivity k is influenced by the thermal conductivity of each distinct phase present in the field (15). The energy transmitted through evaporation and condensation is calculated using the source term S_E.

$$k = \alpha_l k_l + \left(1 - \alpha_l\right) k_v \tag{15}$$

The current work uses the control volume method to discretise the governing equations. The Semi-Implicit Method for Pressure-Linked Equations (SIMPLE) technique couples pressure and velocity. A second-order upwind scheme is used to achieve the spatial discretisation of the momentum and energy equations. The k - ω SST model accounted for the flow field turbulence, which proved accurate and computationally efficient. A solution time step of 10^{-6} was used in order to maintain the courant number less than unity. Further, the value of residuals for continuity, momentum, energy and turbulence model have been set as 1e-6 for accurate results.

3. MESH INDEPENDENT STUDY AND VALIDATION

The mesh-independent study determines the ideal mesh size for an accurate and optimised computation cost. Due to the lack of experimental data for cryogenic two-phase flows, an experimental investigation on air-silicon mixture under room temperature is used to validate the current computational model.

Mesh independent study

An O-grid meshing methodology is used to generate the mesh along the radial direction of the pipe, which can successfully capture the complicated physics in the multiphase flow (Abdulkadir et al., 2015; Chen et al., 2018; Zheng et al., 2019; Agarwal & Dondapati, 2020). Figure 1 shows the structure mesh generated along the longitudinal and radial direction of the pipe where the cluster of mesh has been given near the wall as a large velocity gradient is expected due to the no-slip wall.

For the mesh independence study, four meshes with different sizes were generated with an element size of 40000, 80000, 160000, and 320000, as shown in Fig. 1(b). For the current investigation, a three-dimensional vertical pipe of 50 mm diameter and 1 m length is considered. At the pipe outlet, a plane is considered where the volume

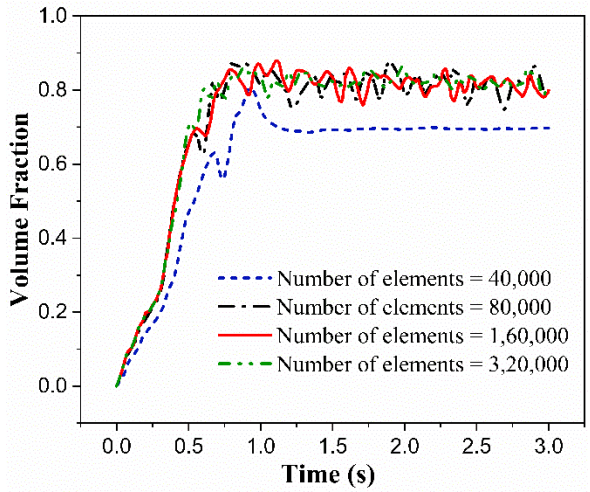

Fig. 2 Volume fraction comparison at outlet of the feed pipe at inlet velocity of 0.4 m/s and temperature of 95 K using four different mesh sizes

Table 2 Specifications and operating conditions of the reference material used for validation

Parameter	(Abdulkadir et al., 2015)
Working fluid (-)	Air-Silicon Mixture
Pipe diameter (mm)	67
Pipe length (m)	6
Working pressure (bar)	1
Operating temperature (K)	293
Inlet liquid velocity (m)	0.05
Inlet vapor velocity (m)	0.344
Inlet volume fraction of vapor (-)	0.873

fraction has been plotted from time t = 0 to 3 sec for all the meshes. It is clear from Fig. 2 that the volume fraction for mesh element sizes of 160000 and 320000 shows similar results after 1s. Hence, the mesh with an element size of 160000 is suited to produce accurate results with the least computation cost.

Validation of the Computational Model

The validation of the computational model is conducted by comparing the computational results with the experimental results. As experimental works on scare, the current validation uses the air and silicon mixture (Abdulkadir et al., 2015) to validate the volume fraction. The operating conditions and geometrical specifications used for the validation study are shown in Table 2. Further, the air-silicone mixture's thermophysical properties that were taken into consideration are given in Table 3.

A plane is made at 1 m from the inlet to compare the volume fraction with experimental results. Figure 3 shows the trace of volume fraction comparison between the computed and experimental results. It is found that the current computational model accurately captures the volume fractions at 1m from the inlet, which shows that the current computational model can be used for further analysis.

Table 3 Physical properties of reference gas liquid system (Abdulkadir et al., 2015)

Fluid	Density (kg/m^3)	Viscosity (Pa-s)	Surface tension (N/m)
Air	1.18	0.000018	0.02
Silicone oil	900	0.0053	0.02

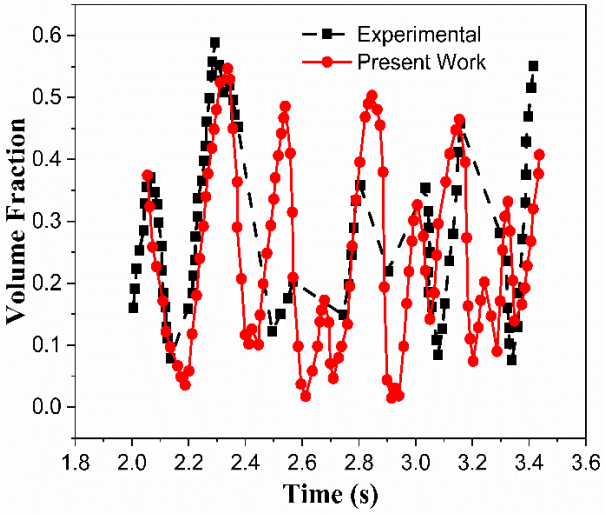

Fig. 3 Comparison of computed Volume fraction with experimental results (Abdulkadir et al., 2015) at 1 m away from inlet for air-silicon oil mixture at the boundary conditions given in Table 2

Table 4 Specifications and operating conditions of the fluid used for validation

Parameter	(Hedayatpour et al., 1993)
Working fluid (-)	Liquid Nitrogen (LN_2)
Outer diameter (mm)	12.7
Inner diameter (mm)	9.5
Pipe length (m)	3.66
Wall temperature (K)	297
Inlet liquid velocity (m)	0.292
Inlet Pressure (kN/m^2)	34.5

Further, another validation is considered using low-temperature cryogenics with liquid nitrogen (LN_2) in a cool-down of a vertical pipe (Hedayatpour et al., 1993). The operating conditions and geometrical specifications utilized for this validation study are given in Table 4. Additionally, Table 5 provides the thermophysical properties of the liquid-vapor nitrogen mixture considered in the analysis.

Figure 4 shows the wall temperature comparison between the computed and experimental results at 90 cm away from the inlet. It is found that the current computational model qualitatively captures the outer wall temperature at 90 cm from the inlet, which shows that the current computational model can be used for further analysis. The underprediction of the temperature may be used for further analysis. The underprediction of the temperature may be due to the limitation of Reynolds-averaged Navier–Stokes equations (RANS equation) that

Table 5 Physical properties of reference gas liquid system (Hedayatpour et al., 1993)

Fluid	Liquid Nitrogen (LN_2)	Vapour Nitrogen (VN_2)
Density (kg/m^3)	806.08	1.138
Viscosity (Pa-s)	0.00016065	0.00001663
Thermal Conductivity (W/m-K)	0.14581	0.0242
Surface Tension (N/m)	0.0089049	

Table 6 The flow conditions used in the current work

Inlet Temperature (K)	Inlet Velocity (m/s)	Inlet Pressure (Pa)	Wall Temperature (K)
95, 100, 105	0.4, 0.7, 1	1.5 *10^5	300

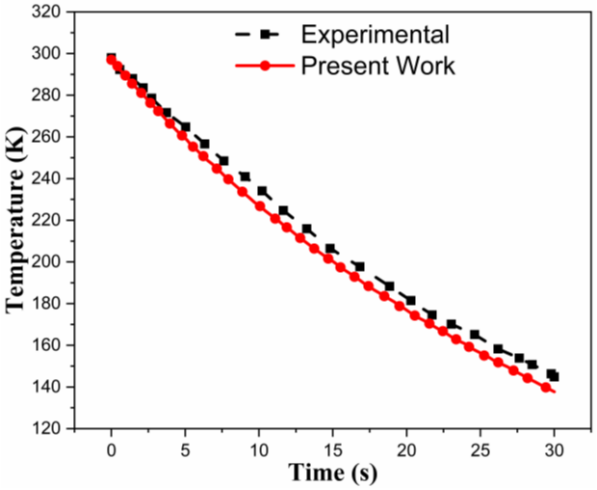

Fig. 4 Comparison of computed temperature with experimental results (Hedayatpour et al., 1993) at 90 cm away from inlet for liquid nitrogen and vapour nitrogen (LN_2 - VN_2) mixture at the boundary conditions given in Table 4

it relies on time-averaging, neglecting some turbulent interactions, and often oversimplifying boundary layer physics.

4. RESULTS AND DISCUSSION

The multiphase flow phenomena in methane feed pipes are investigated using the VOF methodology for the conditions in Table 6. The velocity profile along the radius of the feed pipe, bulk mean temperature (T_b), near wall temperature and mass flow rate are investigated to understand the methane liquid's thermal characteristics and flow dynamics.

The process of hydrodynamic characterisation entails identifying the flow regimes where the two-phase flow phenomena were observed in the feed pipe. When the flow enters from the inlet to the pipe, the liquid methane gets heated by the heated wall and the temperature increases. Once the temperature of liquid methane reaches saturation (T_{SAT} = 116.66 K), the phase change process starts from liquid to vapour. Figure 5 shows the methane vapour volume fraction contour at 3 seconds of flow time at different inlet velocities and temperatures, as shown in Table 6. From the contour, the flow pattern can easily be observed, starting from bubble flow to annular flow followed by slug flow. It is worth mentioning that the multiphase flow pattern may be irregular due to the implementation of gravity conditions in the solver (Kharangate & Mudawar, 2017).

Figures 5(i), 5(ii) and 5(iii) show the methane vapour volume fraction at the inlet velocity of 0.4 m/s and various temperatures of 95K, 100K, and 105K. The methane vapour volume fraction at the 95K temperature is shown in Fig. 5(i), which shows the formation of bubbles well before 0.33 m from the pipe inlet. The radial cross-section (a) in Fig. 5(i) also reveals the vapour formation along the circumference while the liquid is present in the centre of the feed pipe at a particular location in the feed pipe. Further, the coalescence of bubbles is started, and the amount of methane vapour is increased as it reaches section 0.66 m, as shown in Fig. 5(i), while the cross-section (b) reveals that there is no liquid phase available at the location due to phase change. The cross-section (c) on Fig. 5(i) at 1m from the inlet shows that the vapour methane is very high compared to the liquid methane. Fig. 5(ii) shows the vapour volume fraction at 100K of inlet temperature at an inlet velocity of 0.4 m/s. The same phenomena as seen in the previous case are found while the bubble formation is more intense and vapour content is significantly increased, as illustrated by the sections shown in Fig. 5(ii) cross-section (a), cross-section (b), and cross-section (c). Figure 5(iii) shows the vapour volume fraction contour at the 105K wall temperature at an inlet velocity of 0.4 m/s. It was found that the bubble formation was higher than the previous two cases (90K and 100K), which may be due to the higher inlet temperature.

Figures 5(iv)–5(vi) illustrate the methane vapour volume fraction contours at an inlet velocity of 0.7 m/s for three different inlet temperatures of liquid methane. In Fig. 5(iv), at an inlet temperature of 95 K, vapour bubbles are observed to form farther from the feed pipe intake compared to Fig. 5(i). The increased inlet velocity from 0.4 m/s to 0.7 m/s reduces the residence time available for evaporation, leading to a higher concentration of liquid methane at the cross-section (a) in Fig. 5(iv), located 0.33

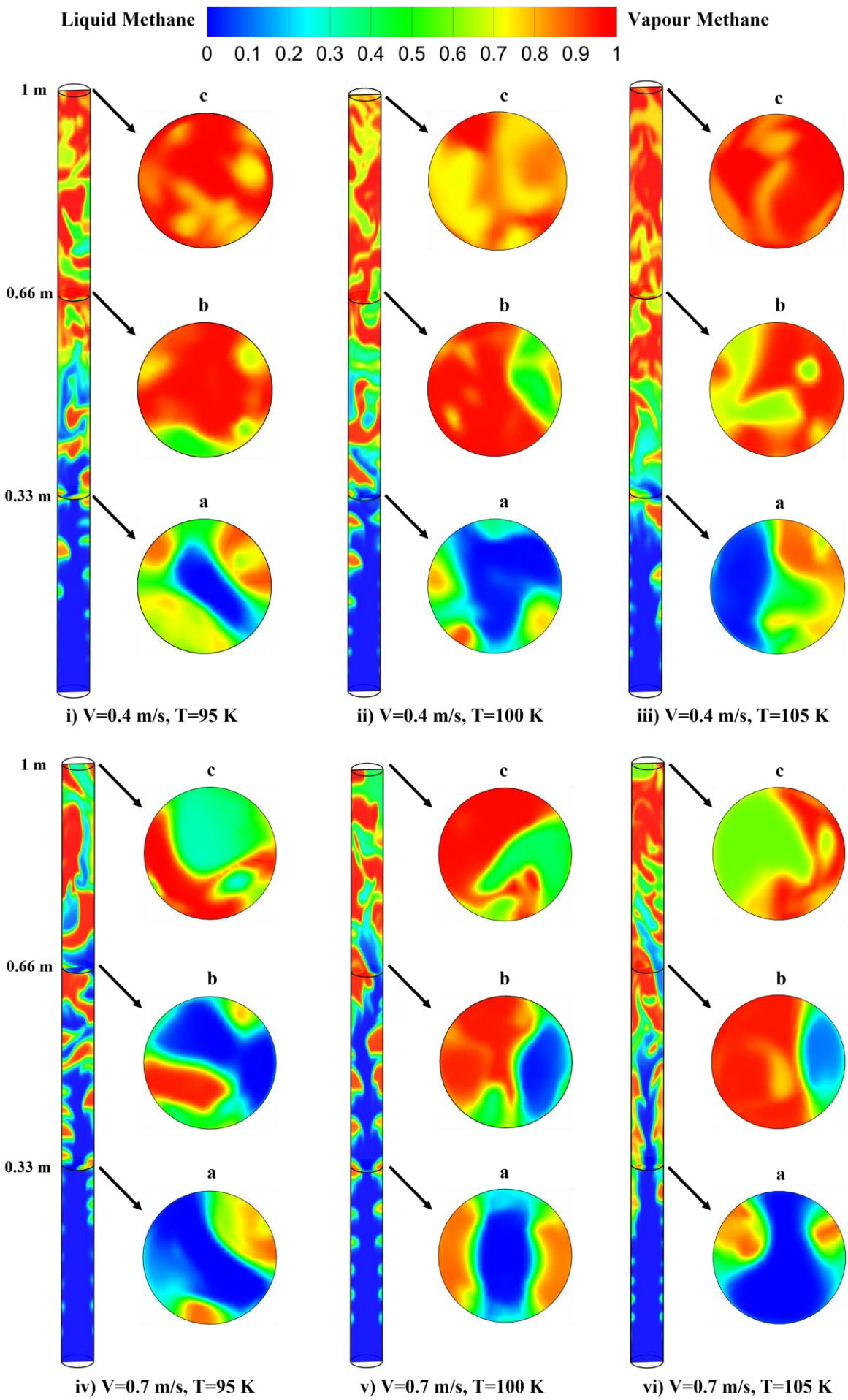
Liquid Methane
Vapour Methane
0 0.1 0.2 0.3 0.4 0.5 0.6 0.7 0.8 0.9 1
1 m
0.66 m
0.33 m
a
b
c
i) V=0.4 m/s, T=95 K
ii) V=0.4 m/s, T=100 K
iii) V=0.4 m/s, T=105 K
iv) V=0.7 m/s, T=95 K
v) V=0.7 m/s, T=100 K
vi) V=0.7 m/s, T=105 K

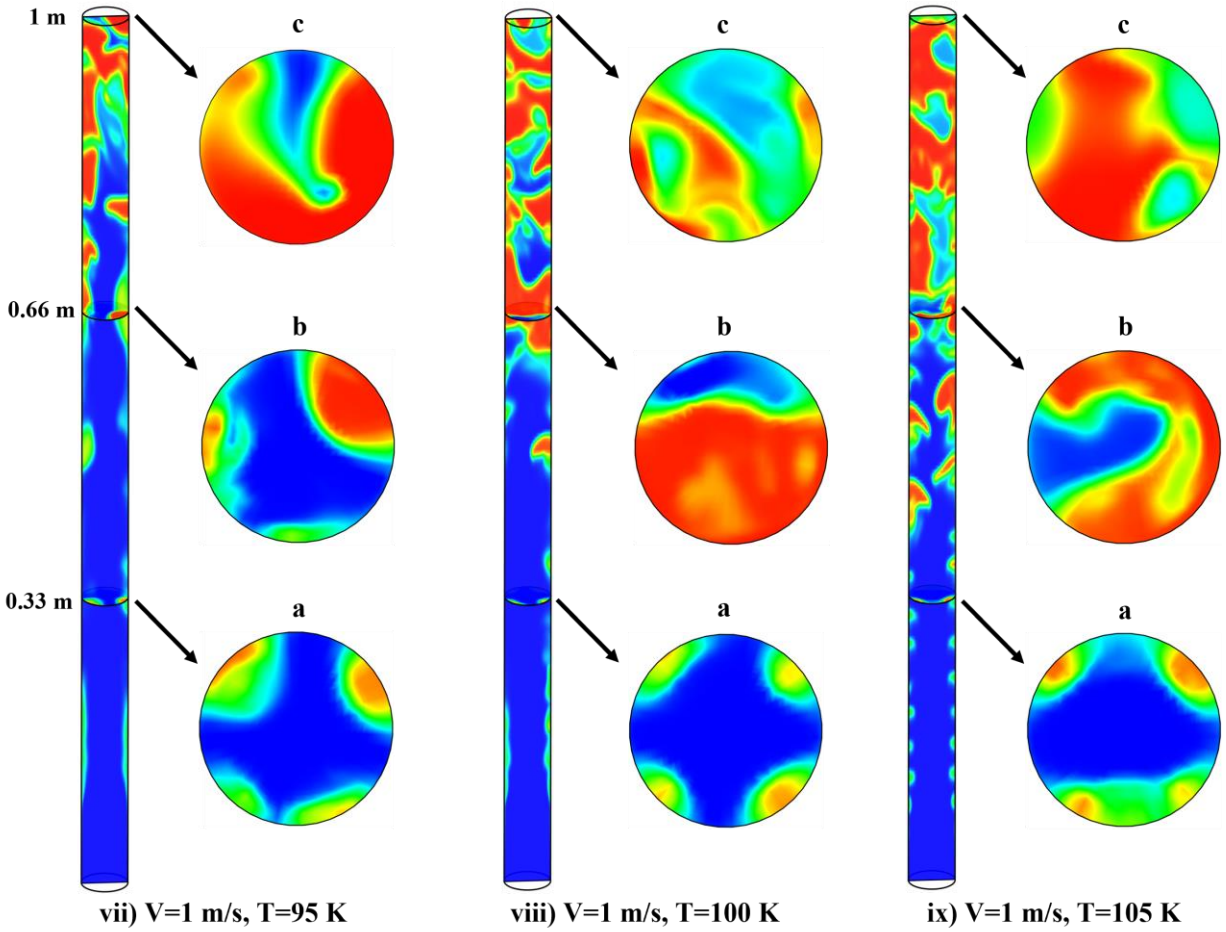

Fig. 5 Volume Fraction contour along the midsection axial as well as radial direction of the feed pipe for wall temperature of 300 K and pressure of 1.5 bar at 3 seconds of the flow for the inlet conditions given in Table 6

m from the inlet, compared to the same location in Fig. 5(i). As the fluid progresses through the feed pipe, the flow transitions from a bubble flow regime to a slug-like flow regime between 0.33 m and 0.66 m from the inlet, resulting in a higher vapour concentration at cross-section (b) of Fig. 5(iv) compared to cross-section (a). Beyond 0.66 m, the flow transitions from slug flow to an annular flow regime, where the outlet cross-section (c) of Fig. 5(iv) shows only methane vapour.

Figure 5(v) illustrates the contour of the VCH_4 volume fraction at an inlet temperature of 100 K. It is observed that the rise in intake temperature from 95 K to 100 K resulted in a higher occurrence of bubble formation, as compared to the findings depicted in Fig. 5(iv). Furthermore, due to the rise in temperature, there was a noticeable shift in the flow pattern of bubble flow, slug flow, and annular flow towards the inlet. Due to this, the increase in vapour methane concentration can be observed from the cross-sectional contour of (a)-(c) in Fig. 5(v). Furthermore, in Fig. 5(vi), a similar flow pattern is observed with more vapour formation due to an increase in inlet temperature to 105 K as illustrated in cross-section (a)-(c) in Fig. 5(vi). Also, the increase in inlet temperature demonstrates that the flow pattern transitions from bubble to slug and subsequently to annular shifted towards inlet compared to the previous two cases shown in Figs 5(iv) and 5(v). These phenomena may be due to the increase in inlet temperature; the critical temperature difference needed for methane vaporisation decreases, increasing methane's vapour formation.

Figure 5(vii) - 5(ix) illustrates the contour of VCH_4 at the inlet velocity of 1 m/s, depicting three distinct inlet temperatures of 95 K, 100 K, and 105 K. Figure 5(vii) demonstrates that the flow regime exhibits a similar pattern to that observed in Fig. 5(i) and 5(iv) at the inlet temperature is 95 K. However, the bubble formation is observed to occur farther downstream from the inlet compared to the previous cases. This behaviour can be attributed to the higher flow velocity, as evident in cross-section (a) of Fig. 5(vii). The increased velocity reduces the residence time for heat transfer, delaying bubble generation and shifting the transition to slug and annular flow regimes further towards the outlet. As a result, liquid methane is still present at 0.66 m from the inlet and even near the outlet, as shown in cross-sections (b) and (c) of Fig. 5(vii). Furthermore, in Fig. 5(viii) at an inlet temperature of 100 K, the flow pattern transitions—bubble flow, slug flow, and annular flow—are noticeably shifted closer to the inlet compared to Fig. 5(vii). This upstream shift is accompanied by an increase in methane vapour concentration across cross-sections (a), (b), and (c) due to the higher inlet temperature enhancing vapour formation.

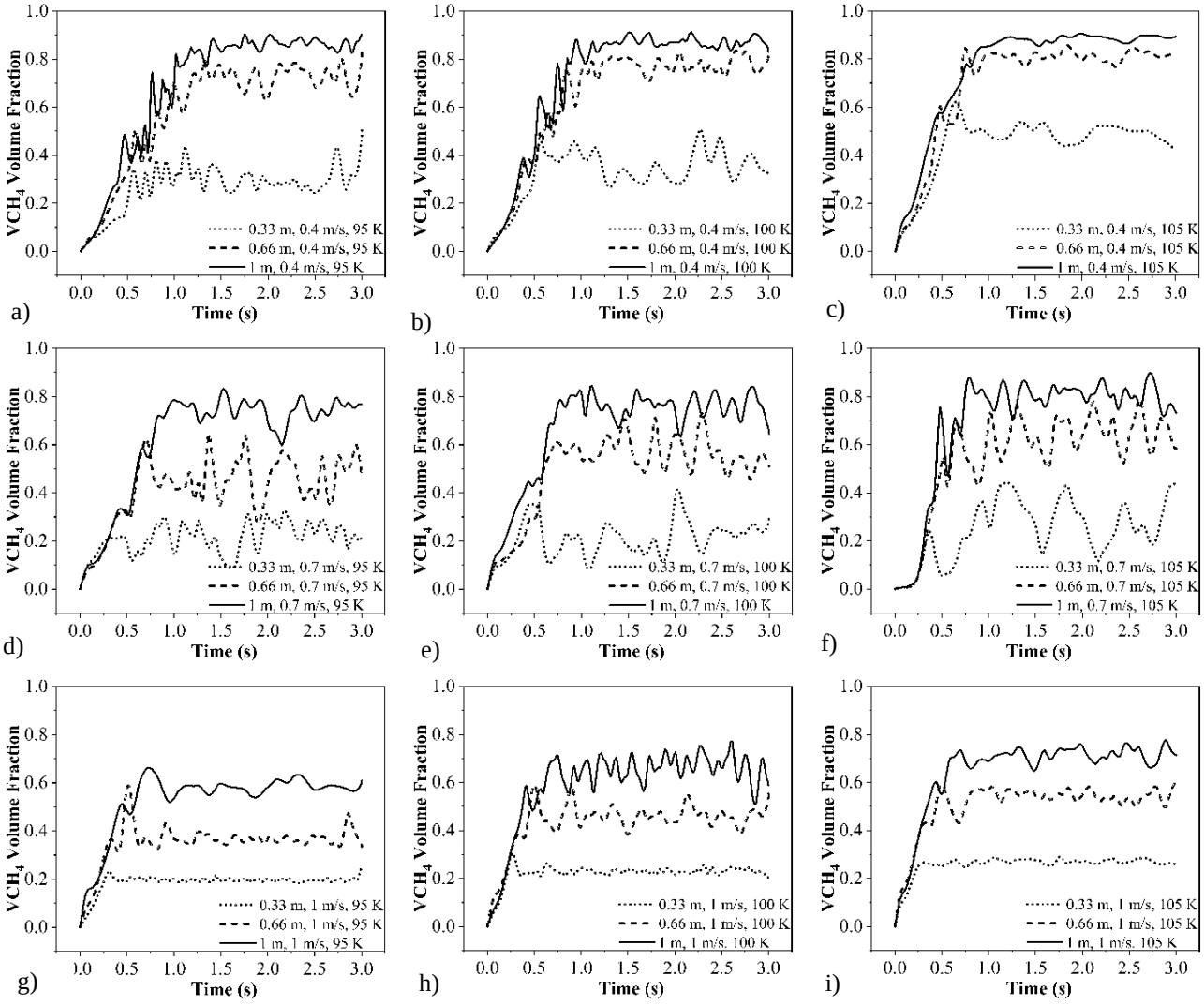

Fig. 6 Average Volume Fraction plot at 0.33 m, 0.66 m from inlet and the outlet with respect to time for wall temperature of 300 K and pressure of 1.5 bar and inlet velocity and temperature of a) 0.4 m/s, 95 K b) 0.4 m/s, 100 K c) 0.4 m/s, 105 K d) 0.7 m/s, 95 K e) 0.7 m/s, 100 K f) 0.7 m/s, 105 K g) 1 m/s, 95 K h) 1 m/s, 100 K i) 1 m/s, 105 K respectively

In Fig. 5(ix), it can be seen that at an inlet temperature of 105 K, the occurrence of bubble flow is significantly closer to the inlet when compared to the previous cases depicted in Fig. 5(vii) and Fig. 5(viii). The cross-sections (a) and (b) in Fig. 5(ix) also show an increased vapour volume fraction due to increased temperature. The slug flow at this temperature is seen just after 0.33 m away from the inlet, which can be easily noticeable in Fig. 5(ix). As the flow passes 0.66 m from the inlet, the flow pattern changes from slug flow to annular flow due to more vapour formation, which may be visualised in cross-section (c) in Fig. 5(ix). The present observation suggests that an increase in the velocity of liquid methane (1 m/s) reduces the interaction time between the fluid and a solid-fluid wall. Further, it is observed that the vapour fraction consistently reduced as the channel length increased, regardless of the inlet temperature (Bhuva et al., 2022).

Figure 6 shows methane vapour's average volume fraction change with respect to time (t) starting from zero to three seconds. At the initial time point ($t = 0s$), the pipe contains solely pure liquid methane, resulting in a volume fraction of zero. Within Fig. 6, the VCH_4 volume fraction profiles are gathered from three distinct locations: specifically, these locations are positioned at 0.33 m and 0.66 m away from the inlet and the outlet. These measurements are taken under varying conditions encompassing different velocities (0.4 m/s, 0.7 m/s, 1 m/s) and temperatures (95 K, 100 K and 105 K). In Fig. 6(a-c), the VCH_4 volume fraction profile is shown at an inlet velocity of 0.4 m/s and three temperatures of 95 K, 100 K and 105 K. It becomes evident that the VCH_4 volume fraction increases linearly from zero until 0.5 seconds due to the occurrence of evaporation at the solid-liquid interface. Figure 6(a) shows the volume fraction at three different locations in the feed pipe at an inlet temperature of 95 K. It is seen that at a location situated 0.33 m from the inlet, the volume fraction traces reveal a maximum value of 0.42, attributed to the presence of bubbles flowing within the feed pipe. Similarly, the volume fraction trace at the location 0.66 m from the inlet increases up to 0.81, which can be attributed to the transformation from bubble flow to slug flow within the feed pipe. Moreover, at the outlet, we observe a maximum VCH_4 volume fraction of

0.91, indicating the substantial conversion of liquid into vapour due to annular flow.

Figure 6(b) shows the VCH_4 volume fraction plot for an inlet velocity of 0.4 m/s and a temperature of 100 K. The volume fraction profiles at three distinct positions, 0.33 m and 0.66 m from the inlet and outlet, exhibit a similar pattern as observed in Fig. 6(a). Notably, the intensity of bubble flow, slug flow, and annular flow is increased due to the increase in the inlet temperature, which consequently leads to a rise in the volume fraction of vapour methane. Figure 6(c) displays the VCH_4 volume fraction plot under conditions of an inlet velocity of 0.4 m/s and a temperature of 105 K. At this temperature, a reduction in the difference in the evaporation temperature of the fluid results in maximum volume fractions of 0.60 at 0.33 m from the inlet, 0.81 at 0.66 m from the inlet, and an impressive 0.93 at the outlet. The increase in inlet temperature and its subsequent effect on the difference in evaporation temperature notably influence the distribution of vapour methane, which is easily notable in the volume fraction profiles along the pipe.

Figure 6(d) - 4(f) illustrates the variation in VCH_4 volume fraction at an input velocity of 0.7 m/s, showcasing three various inlet temperatures of 95 K, 100 K, and 105 K. It has been observed that the increase in the initial velocity of the feed pipe leads to a decrease in the volume fraction of VCH_4 with time. The decrease in heat absorption by the liquid from the feed pipe may be attributed to increased intake velocity. The reduction in heat absorption results in the reduction of the vaporisation process, causing a decline in the volume fraction of VCH_4. Fig. 6(d) shows that at the inlet velocity of 0.7 m/s and temperature of 95 K, the VCH_4 volume fraction traces at a distance of 0.33 m from the inlet exhibit a maximum volume fraction of 0.3, which may be owing to bubble flow occurring within the feed pipe. The observation of a maximum vapour volume percentage of 0.64 at a distance of 0.66 m from the inlet suggests the presence of a slug flow pattern within the flow regime.

Further, it was observed that the annular flow pattern becomes prominent in the feed pipe as the fluid flow progresses towards the pipe outlet. These phenomena can be observed by examining the vapour volume fraction at a plane near the outlet of the feed pipe, where the highest volume fraction of VCH_4 is 0.81. Figure 6(e) displays the plot of VCH_4 volume percentage at an intake velocity of 0.7 m/s and a temperature of 100 K. The volume fraction profiles were examined at three specific positions: 0.33 m and 0.66 m from the inlet and the exit. It was noticed that the significant volume fraction of VCH_4 at these locations were 0.37, 0.70, and 0.82, respectively, which demonstrate a similar pattern to Fig. 6(d). It is worth mentioning that the intensity of bubble flow, slug flow, and annular flow is amplified due to an increase in the inlet temperature, which consequently leads to an elevation in the volume fraction of vapour methane. Further, Fig. 6(f) displays the VCH_4 volume fraction plot under conditions of an inlet velocity of 0.7 m/s and a temperature of 105 K. At this temperature, a reduction in the difference in the evaporation temperature of the fluid results in maximum volume fractions of 0.42 at 0.33 m from the inlet, 0.73 at 0.66 m from the inlet, and an impressive 0.88 at the outlet.

Figure 6(g) - 6(i) illustrates the behaviour of VCH_4 volume fraction within a dynamic fluid system, where the inlet velocity is held constant at 1 m/s, while three distinct inlet temperatures, namely 95 K, 100 K, and 105 K, are investigated. Due to a further increase in inlet velocity to 1 m/s in the feed pipe, there is a reduction in the VCH_4 volume fraction with time. The reduction in the VCH_4 volume fraction may be due to the accelerated inlet velocity at 1 m/s limiting the interaction time between the liquid and the heat source in the feed pipe. As a consequence, the heat absorption capacity of the liquid is getting slow, leading to a reduction in the vaporisation rate. Moreover, increased inlet velocity disrupts the physics of thermal forces within the liquid-gas mixture. Normally, vaporization occurs at the boundary between the liquid and gas phases, and the establishment of a stable boundary relies on the equilibrium of thermal energy. The increase in inlet velocity disrupts the equilibrium and reduces the vaporization which leads to a decrease in the VCH_4 volume fraction (Zheng et al., 2019).

Further, Fig. 6(g) shows the average volume fraction at an inlet temperature of 95 K and velocity of 1m/s. It may be seen that at 0.33 m away from the inlet, the bubble formation occurs with a volume fraction of 0.22. However, the increase in vapour volume fraction to 0.59 was observed at a distance of 0.66 m from the inlet, indicating that a slug flow pattern predominated within the flow regime. An annular flow pattern is established as the two-phase fluid moves towards the pipe's outlet, as indicated by the highest VCH_4 volume fraction of 0.67. Figure 6(h) shows the VCH_4 volume fraction at an input velocity of 1 m/s and a temperature of 100 K. At 0.33 m and 0.66 m from the inlet and the exit, similar patterns of Fig. 6(g) are seen, with maximum VCH_4 volume fractions of 0.29, 0.56, and 0.77, respectively. It is worth mentioning that the intensity of bubble flow, slug flow, and annular flow is amplified due to an increase in the inlet temperature, which consequently leads to an elevation in the volume fraction of vapour methane. The VCH_4 volume fraction at 1 m/s inlet velocity and 105 K temperature is shown in Fig. 6(i). It is evident that the maximum volume fraction at the outlet of the feed pipe is 0.79, which is lower at 105 K compared to previous cases with the same temperature, as shown in Figs 6(c) and 6(f). This reduction in volume fraction at the outlet may be owing to the increase in inlet velocity. However, it is found that the volume fraction at 0.33 m and 0.66 m locations are relatively higher than 95 K and 100 K inlet temperature cases, as shown in Figs 6(g) and 6(h).

The temperature distribution along the pipe length is analysed at various inlet temperatures and velocities to get temperatures of 95K, 100K, and 105K. It is seen that the increase in inlet temperature leads to fewer bubble traps in the flow regime, which may be easily noticed in Fig. 7(i (a-c)). Further, in Fig. 7(ii), at the inlet velocity of 0.7 m/s, the temperature inside the feed pipe decreases compared with Fig. 7(i). Finally, Fig. 7(iii) shows the temperature distribution along the pipe length at a velocity of 1m/s. The results show that the temperature inside the pipe

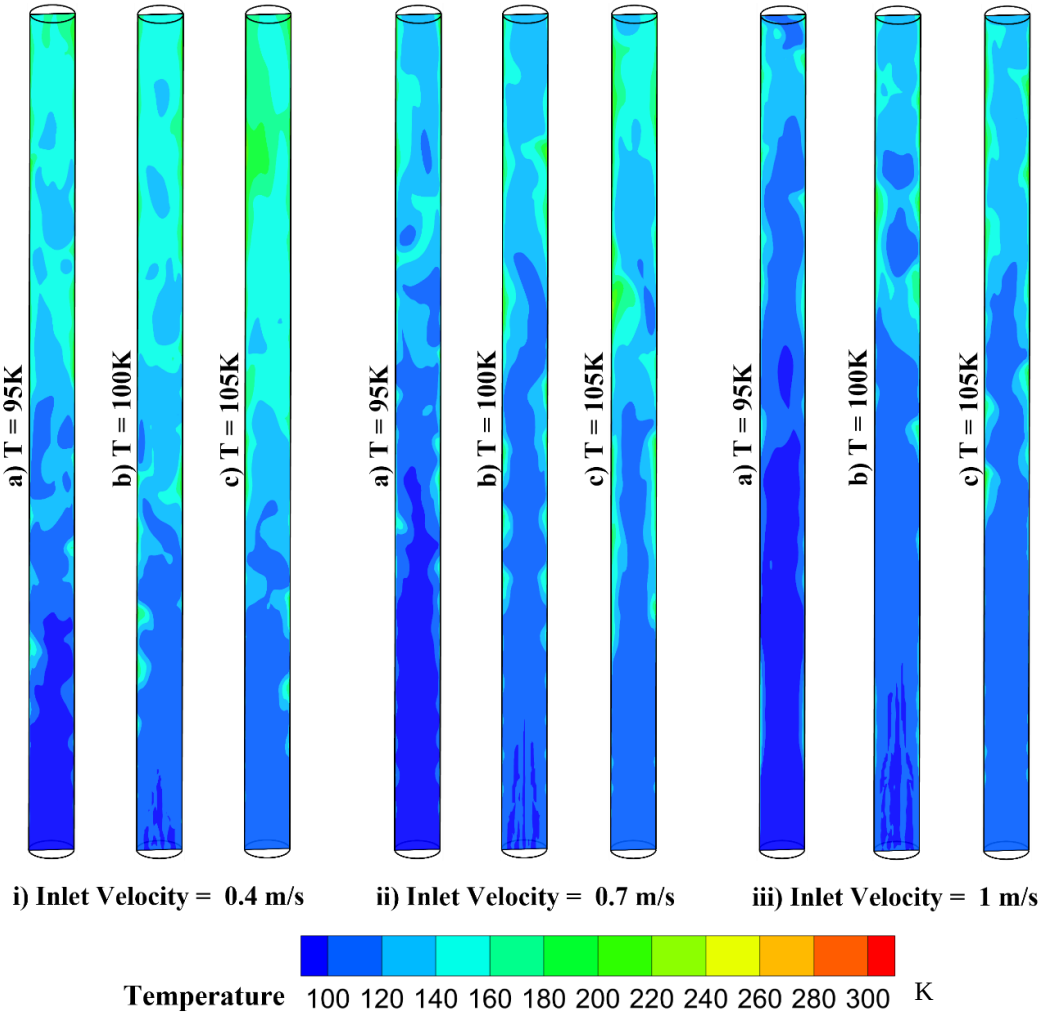

Fig. 7 Temperature contour at the midsection axial length of pipe for wall temperature and pressure of 300 K and 1.5 bar, respectively, at 3 seconds of flow with i) inlet velocity 0.4 m/s and temperatures of a) 95 K, b) 100 K, c) 105 K ii) inlet velocity 0.7 m/s and temperatures of a) 95 K, b) 100 K, c) 105 K iii) inlet velocity 1 m/s and temperatures of a) 95 K, b) 100 K, c) 105 K

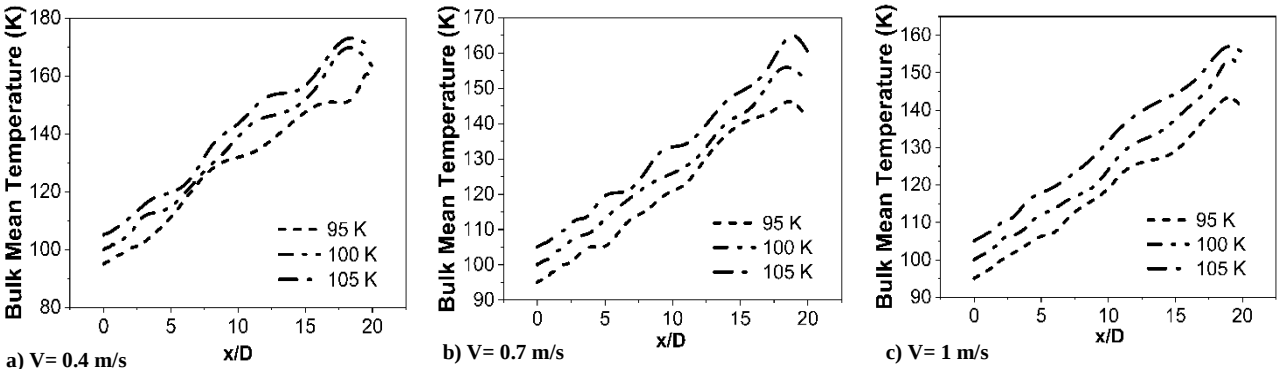

Fig. 8 Bulk mean temperature plot along the non-dimensional length of the pipe at 3 seconds for a wall temperature of 300 K and pressure of 1.5 bar for a) inlet velocity of 0.4 m/s and temperatures of 95 K, 100 K and 105 K b) inlet velocity 0.7 m/s and temperatures of a) 95 K, b) 100 K, c) 105 c) inlet velocity 1 m/s and temperatures of a) 95 K, b) 100 K, c) 105 K

decreases when compared with the previous two cases (Fig. 7(i) and 7(ii)). The physical significance behind that is the temperature gradient in the boundary layer causes fluid flow and mixing, reducing the temperature difference between near and far surfaces and causing a decrease in fluid temperature as you move away from the wall. The rate of temperature decrease depends on fluid properties, velocity, and solid surface geometry.

Figure 8 shows the bulk mean temperature (T_b) plot as a function of the non-dimensional pipe length (x/D) at

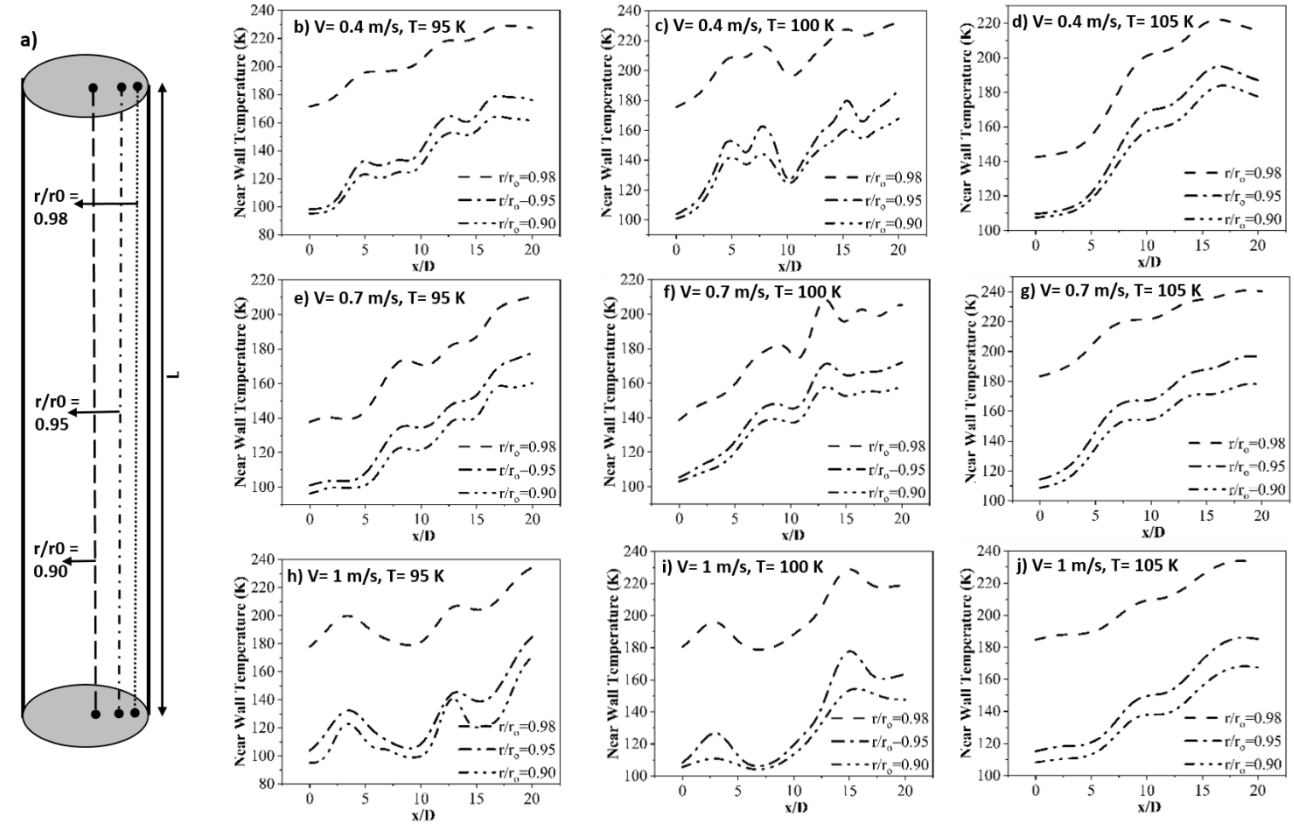

Fig. 9 Near wall temperature at a) r/r0 = 0.98, 0.95, 0.90 plot along the non-dimensional length at 3 seconds of flow for wall temperature of 300 K and pressure of 1.5 bar and inlet velocity and temperature of b) 0.4 m/s, 95 K c) 0.4 m/s, 100 K d) 0.4 m/s, 105 K e) 0.7 m/s, 95 K f) 0.7 m/s, 100 K g) 0.7 m/s, 105 K h) 1 m/s, 95 K i) 1 m/s, 100 K j) 1 m/s, 105 K respectively

various inlet velocities and temperatures. In Fig. 8(a), the bulk mean temperature increase along the longitudinal length of the pipe is observed at an inlet velocity of 0.4 m/s. The maximum bulk mean temperature observed for an inlet temperature of 105 K is 176 K, which is higher when compared with the 95 K and 100 K inlet temperatures. In the subsequent analysis, as depicted in Fig. 8(b), at the inlet velocity of 0.7 m/s, the bulk mean temperature is 168 K for the inlet temperature of 105 K, which is higher when compared with 100 K and 95 K inlet temperature cases. Finally, Fig. 8(c) shows the bulk mean temperature along the pipe at 1m/s inlet velocity; the highest bulk mean temperature is observed as 158 K at the inlet temperature of 105 K. The observed phenomenon can be attributed to the direct relationship between the average temperature and the volume fraction of VCH_4.

The time average temperature near the pipe wall at three different radial locations r/r0=0.98, 0.95 and 0.90 (as shown in Fig. 9(a)) has been analyzed for the inlet velocity of 0.4 m/s, 0.7 m/s and 1 m/s and the inlet temperature of 95 K, 100 K and 105 K at 3 seconds of the flow time as shown in Fig. 9. At 0.4 m/s of inlet velocity and 95K of inlet temperature, it is seen from Fig. 9(b) that the near wall temperature increases to 150K at r/r0 = 0.90 while the temperature reaches 170K at r/r0 = 0.95 and 230K at r/r0 = 0.98. Figure 9(c) shows the temperature at inlet velocity and temperature, 0.4 m/s and 100 K, respectively. The results at the radial distance of r/r0 = 0.90, r/r0 = 0.95, and r/r0 = 0.98 show the maximum temperature rise of 162 K, 180 K and 232 K, respectively, which is in similar trends as seen in Fig. 9(b). At an inlet velocity and temperature of 0.4 m/s and 105 K, as shown in Fig. 9(d), the temperature increases linearly from the inlet to the outlet of the feed pipe. Further, at a radial distance of r/r0 = 0.90, r/r0 = 0.95, and r/r0 = 0.98, the maximum near-wall temperature is 175 K, 185 K, and 220 K, respectively.

Further, Fig. 9(e) shows the temperature, inlet velocity, and temperature of 0.7 m/s and 95 K, respectively. At r/r0 = 0.90, r/r0 = 0.95 and r/r0 = 0.98, the maximum temperature reaches 152 K, 168 K and 209 K, respectively, with similar trends as a previous case in Fig. 9(b). Figure 9(f) shows the temperature at inlet velocity and temperature of 0.7 m/s and 100 K, respectively, where it is seen that at a radial distance of r/r0 = 0.90, r/r0 = 0.95 and r/r0 = 0.98, the maximum temperature reaches to 155 K, 170 K and 210K respectively. Similarly, Fig. 9(g) shows the temperature along the pipe length at r/r0 = 0.90, r/r0 = 0.95 and r/r0 = 0.98 for the inlet velocity of 0.7m/s and inlet temperature of 105 K. It is found that the maximum temperature at r/r0 = 0.90, r/r0 = 0.95 and r/r0 = 0.98 are 170 K, 190 K and 240 K, respectively.

Figure 9(h) shows the temperature at inlet velocity and temperature of 1 m/s and 95 K. At three different radial locations, i.e., r/r0 = 0.90, r/r0 = 0.95 and r/r0 = 0.98, the maximum near-wall temperature reaches to 169 K, 182 K and 232 K respectively. Similar phenomena have been seen in Fig. 9(i), where at an inlet temperature of 100 K,

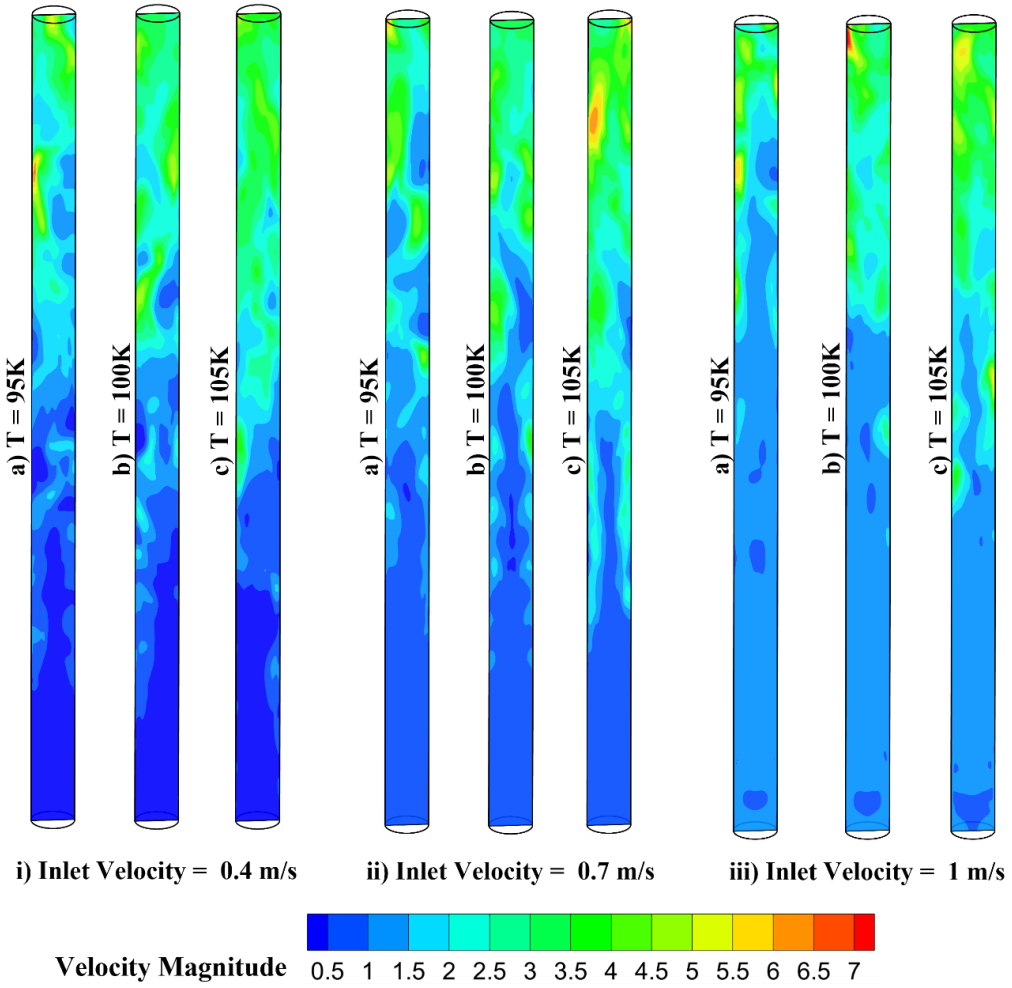

Fig. 10 Velocity contour at the midsection axial length of pipe for wall temperature and pressure of 300 K and 1.5 bar, respectively, at 3 seconds of flow with i) inlet velocity 0.4 m/s and temperatures of a) 95 K, b) 100 K, c) 105 K ii) inlet velocity 0.7 m/s and temperatures of a) 95 K, b) 100 K, c) 105 K iii) inlet velocity 1 m/s and temperatures of a) 95 K, b) 100 K, c) 105 K

the maximum temperature at r/r0 = 0.90, r/r0 = 0.95 and r/r0 = 0.98 are 151 K, 174 K and 230 K, respectively. In Fig. 9(j), at an inlet temperature of 105 K, similar trends have been seen while the maximum temperature at a radial distance of r/r0 = 0.90, r/r0 = 0.95 and r/r0 = 0.98 are 167 K, 185 K and 232 K respectively. The time average near-wall temperature reveals consistent trends along the radial locations at various inlet velocities and temperatures. However, in Fig. 9, at lower inlet velocity and higher inlet temperatures, a noticeable increase in near-wall temperatures is observed, with the temperature reaching higher values towards the outlet of the feed pipe. Also, due to the increase in inlet velocity, there is an increase in the near-wall temperature due to an increase in turbulence in the fluid domain (Wang et al., 2010).

Figure 10 illustrates the contour of the magnitude of mixture velocity at 3 seconds of the flow time along the pipe's longitudinal axis. Figure 10(i) shows the mixture velocity contour at an inlet velocity of 0.4 m/s and various temperatures of 95 K, 100 K, and 105 K. It is evident from the contour that the velocity of the two-phase flow within the conduit increases as the inlet temperature rises. Similarly, it can be observed from Fig. 10(ii) that the velocity of the mixture increases when the inlet velocity is raised to 0.7 m/s, compared to Fig. 10(i). The observed phenomenon can be attributed to the augmentation in the inlet velocity increasing turbulence. The turbulence has the potential to influence the dispersion and motion of vapour bubbles within the liquid phase, consequently exerting an impact on the velocity of the mixture. As previously stated, the increase in inlet temperature from 95 K to 105 K resulted in a corresponding increase in mixture velocity. As depicted in Figure 10(iii), it is observed that the increase in inlet velocity and temperature results in a corresponding increase in the mixture velocity (Lee et al., 2022).

Figure 11 shows the velocity magnitude at mid-plane, i.e., at 0.5 m away from the inlet, and the outlet for all three velocities and temperature at 3 seconds of flow. Figure 11(a) illustrates the specific positions along the feed pipe at which the velocity magnitude is plotted. Figure 11(b) presents the velocity magnitude along the radial length for an inlet velocity of 0.4 m/s. It is observed that the minimum velocity of 1.4 m/s and maximum velocity

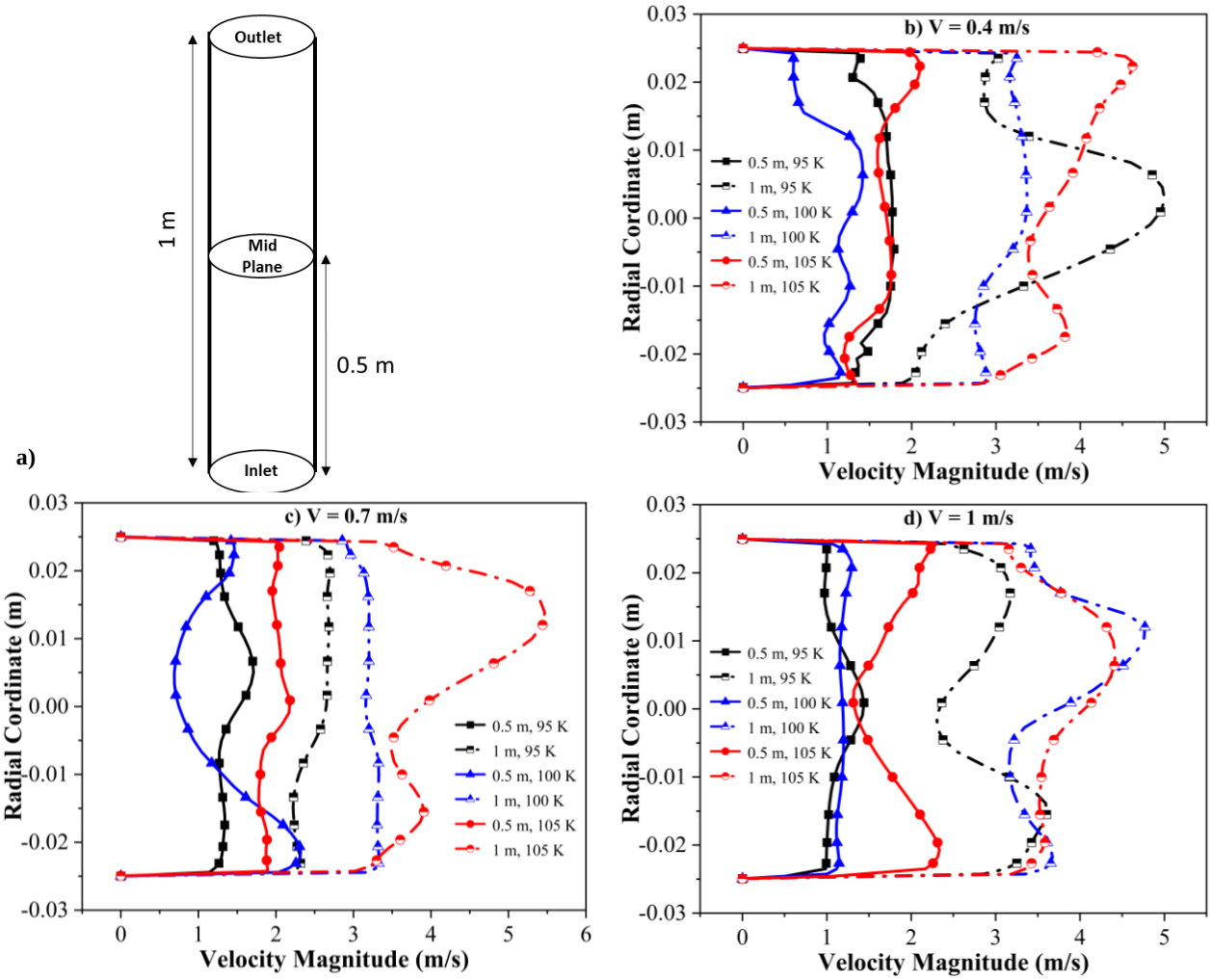

Fig. 11 Velocity magnitude at a) mid-plane and outlet of the pipe after 3 seconds of flow, with a wall temperature of 300 K, a pressure of 1.5 bar, and inlet temperatures of 95 K, 100 K, and 105 K, for inlet velocities of b) 0.4 m/s, c) 0.7 m/s, and d) 1 m/s

of 1.9 m/s at the mid-plane were obtained at inlet temperatures of 95 K and 105 K, respectively. The present study observed that the minimum velocity of 3.3 m/s was recorded at the outlet of the feed pipe at inlet temperature conditions of 100K. Furthermore, at 95 K and 105 K inlet temperatures, the maximum velocity magnitude was approximately 4.95 m/s and 4.83 m/s, respectively. The underlying physical phenomenon can be attributed to the expansion and decrease in the vapour phase's density as the fluid's temperature rises. The phenomenon mentioned above may lead to a reduction in the overall density of the fluid, consequently resulting in an augmentation of the fluid's velocity. The phenomenon under consideration is called the "thermal expansion" effect (Kharangate & Mudawar, 2017). Figure 11(c) exhibits the velocity magnitude for a flow rate of 0.7 m/s. The plot reveals that the highest velocity at the mid-plane is 2.2 m/s, observed at an inlet temperature of 105 K. Moreover, at the outlet of the feed pipe, a velocity of 5.6 m/s is attained at an inlet temperature of 105 K. Figure 11(d) depicts the velocity magnitude at an inlet velocity of 1 m/s, with a mid-plane velocity of 2.4 m/s at an inlet temperature of 105 K and the velocity magnitude is 4.95 m/s at the outlet for the inlet temperature of 100 K.

The mass flow rate of a two-phase flow, namely liquid-vapor flow, can be influenced by temperature and velocity more sophisticatedly than single-phase flows. This complexity arises primarily from the intricate interplay between the two phases (Wu et al., 2017). Figure 12 shows liquid and vapour methane's average mass flow rates along the pipe's non-dimensional length (x/D). Increasing the inlet velocity generally leads to an increase in the mass flow rate of LCH_4 in a general sense. In Fig. 12(a), at the inlet velocity of 0.4 m/s, the initial mass flow rate of LCH_4 is 0.33 kg/s. Further, it is seen that the liquid methane mass flow rate steadily decreases as the fluid passes through the pipe owing to the vapour formation caused by multiphase phenomena. At the inlet of the pipe, the mass flow rate of VCH_4 is zero for all the inlet temperatures, and it reached 0.0041 kg/s at the outlet for the inlet temperature of 105 K, while the others are a little less. This observation indicates that the maximum vapour formation occurs when the intake velocity is 0.4 m/s, and the inlet temperature is 105 K.

In Fig. 12(b), the inlet velocity is raised to 0.7 m/s, and it is found that the LCH_4 flow rate at the inlet escalated to 0.58 kg/s. However, the VCH_4 flow rate diminishes at the outlet, falling below 0.004 kg/s compared to the 0.4

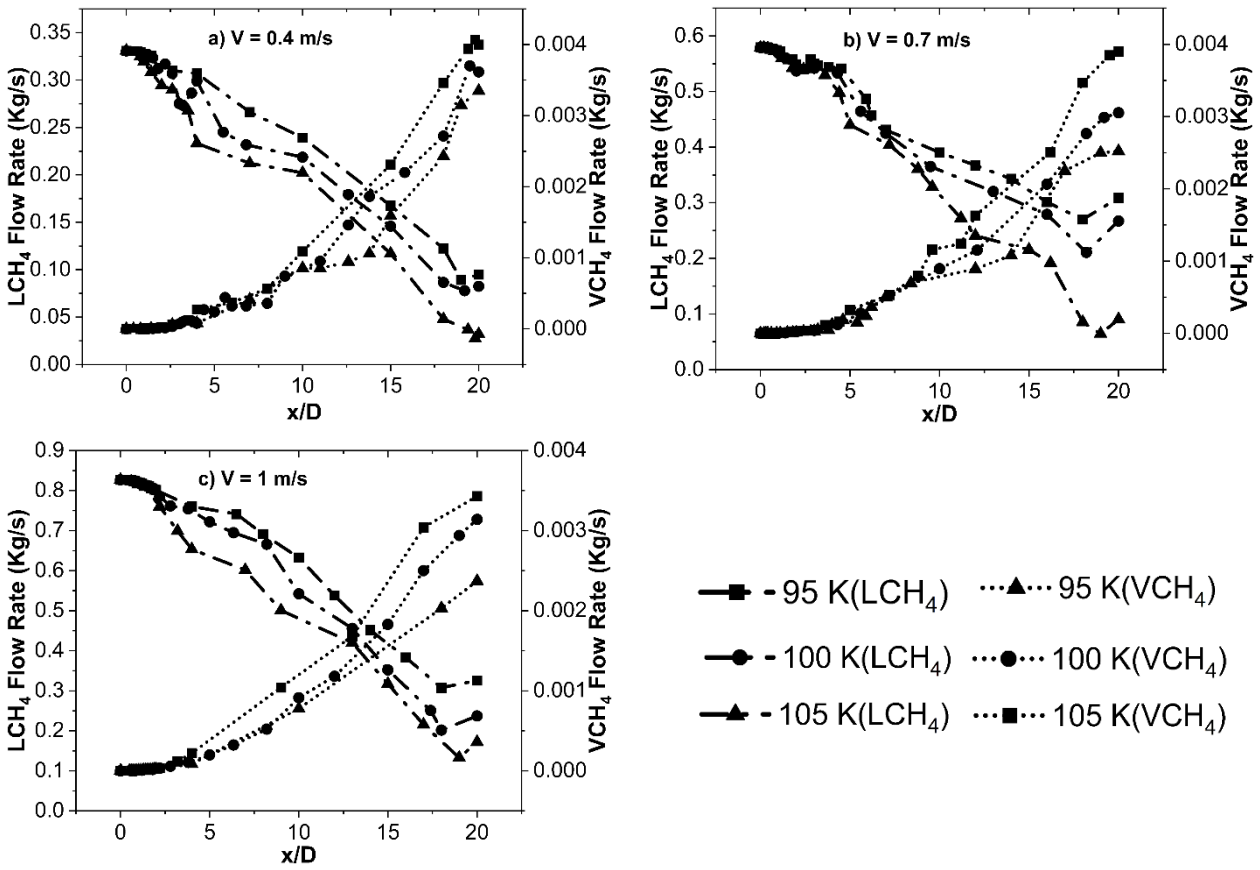

Fig. 12 Flow rate plot of liquid and vapour methane along the non-dimensional length of pipe flow for wall temperature of 300 K, pressure of 1.5 bar, and inlet velocity of a) 0.4 m/s, b) 0.7 m/s and c) 1 m/s

m/s cases. This decrease in VCH_4 flow rate can be attributed to the fact that at higher velocities, the two phases tend to segregate more, and increasing the velocity can leave a greater portion of the liquid phase behind, ultimately causing a decrease in the mass flow rate of the vapor phase. Subsequently, in Fig. 12(c), the LCH_4 and VCH_4 flow rates at an inlet velocity of 1 m/s are shown. The LCH_4 flow rate at the inlet reaches its highest point at 0.84 kg/s while the vapour formation at the outlet of the feed pipe drops below 0.0035 kg/s, less than in the previous two cases. Notably, the minimum vapour formation, at 0.0023 kg/s, occurs at an inlet velocity and temperature of 1 m/s and 95 K, respectively.

Furthermore, raising the temperature can increase the vaporisation of the liquid phase, resulting in an upsurge in the mass flow rate of the vapour. This phenomenon is evident in Fig. 12, where, for all three cases, the VCH_4 mass flow rate shows an increase as the inlet temperature rises from 95 K to 105 K. Excessive temperature increases can cause the liquid to entirely vaporise, which, in turn, can reduce the mass flow rate due to the absence of the liquid phase.

5. CONCLUSION

The current study focuses on the hydrodynamic and thermodynamics analysis of the multiphase flow of LCH_4-VCH_4 in a vertical pipe flow. The three-dimensional cryogenic feed pipe for multiphase flow is modelled using the VOF model and the energy equation for hydrodynamic and thermodynamics characterization. The feed pipe is constantly heated with an ambient temperature of 300 K throughout the pipe's length, which has dimensions of 50 mm diameter and 1 m length. The results, such as volume fraction, bulk mean temperature, wall temperature, velocity magnitude, and mass flow rate, are analysed in two-phase flow dynamics of liquid methane.

The volume fraction results of VCH_4 clearly show the formation of bubble flow growth near the inlet as the liquid temperature reaches the saturation temperature. As the bubble grows with time, coalescence starts occurring, which leads the bubbles to merge and grow into larger bubbles, leading to slug flow. Then, the flow becomes annular due to the flow rate, geometry, and fluid properties. It is seen that increasing the inlet temperature at a particular velocity will increase the volume fraction at a faster rate, while the maximum volume fraction is not affected at low velocity. The findings indicate that increasing the inlet temperature at a given velocity accelerates the rise in methane vapor volume fraction, with a marked increase of 25-30% when the inlet temperature is raised from 95 K to 105 K. On the other hand, at higher fluid velocities (0.7 m/s and 1 m/s), the phase changes shift further downstream, as reduced interaction time with the heated wall delays bubble formation and vaporization.

It is observed that the bulk mean temperature of the multiphase methane is decreased with an increase in velocity due to a reduced heat transfer rate. The maximum

bulk mean temperatures of 176 K, 168 K, and 158 K were observed at inlet temperatures of 105 K for velocities of 0.4 m/s, 0.7 m/s, and 1 m/s, respectively. Further, it may be seen that raising the inlet temperature in a two-phase flow system significantly enhances mixture velocity. For an inlet velocity of 0.4 m/s, the mixture velocity increases from 1.4 m/s at 95 K to 1.9 m/s at 105 K, with outlet velocities of 4.95 m/s and 4.83 m/s, respectively. This enhancement is due to thermal expansion, which reduces fluid density and increases flow velocity. At higher inlet velocities of 0.7 m/s and 1 m/s, mid-plane velocities reach 2.2 m/s and 2.4 m/s at 105 K, while outlet velocities peak at 5.6 m/s and 4.95 m/s. Moreover, an increase in inlet velocity causes a decrease in the vapour flow rate, but a significant increase in the vapour flow rate can be observed at higher temperatures when the inlet velocity remains constant.

Overall, the obtained multiphase flow characteristics indicate that transporting liquid methane through the feed pipe requires extra attention because of the unpredictable behaviour of the two-phase flow. Implementing advanced multiphase flow modelling and simulation tools is essential for predicting velocity, temperature, flow regimes, and potential instabilities in methane pipelines. Additionally, incorporating safety margins and robust monitoring systems will help mitigate risks and facilitate rapid responses to changes in flow characteristics during operation. Further, an investigation of multiphase phenomena on the regenerative cooling in rocket engines may be interesting owing to the hot gas mixture and methane liquid. Also, it is essential for designing a cryogenic storage tank where the Boil-off may occurs. Moreover, a multiphase study on methane liquid droplet surface impact may give more insight into multiphase phenomena and droplet dynamics of methane liquid. We hope to report the investigation of these challenging subjects in the near future.

CONFLICT OF INTEREST

The authors declare that they have no conflict of interest.

AUTHORS CONTRIBUTION

Kanak Raj contributed to the problem formulation, numerical model setup, validation, data analysis, draft writing; **Prince Raj Lawrence Raj** supervised the numerical analysis, data interpretation and draft revision.

REFERENCES

Abdulkadir, M., Hernandez-Perez, V., Lo, S., Lowndes, I. S., & Azzopardi, B. J. (2015). Comparison of experimental and Computational Fluid Dynamics (CFD) studies of slug flow in a vertical riser. *Experimental Thermal and Fluid Science*, *68*, 468–483. https://doi.org/10.1016/j.expthermflusci.2015.06.004

Agarwal, R., & Dondapati, R. S. (2020). Numerical investigation on hydrodynamic characteristics of two-phase flow with liquid hydrogen through cryogenic feed lines at terrestrial and microgravity. *Applied Thermal Engineering*, *173*(September 2019), 115240. https://doi.org/10.1016/j.applthermaleng.2020.115240

Ahammad, M., Olewski, T., Véchot, L. N., & Mannan, S. (2016). A CFD based model to predict film boiling heat transfer of cryogenic liquids. *Journal of Loss Prevention in the Process Industries*, *44*, 247–254. https://doi.org/10.1016/j.jlp.2016.09.017

Al Ghafri, S. Z. S., Swanger, A., Jusko, V., Siahvashi, A., Perez, F., Johns, M. L., & May, E. F. (2022). Modelling of liquid hydrogen boil-off. *Energies*, *15*(3). https://doi.org/10.3390/en15031149

Antar, B. N., & Collins, F. G. (1995). *Vertical line quench in low gravity.* 33rd Aerospace Sciences Meeting and Exhibit. https://doi.org/10.2514/6.1995-698

Archipley, C., Barclay, J., Meinhardt, K., Whyatt, G., Thomsen, E., Holladay, J., Cui, J., Anderson, I., & Wolf, S. (2022). Methane liquefaction with an active magnetic regenerative refrigerator. *Cryogenics*, *128*(October), 103588. https://doi.org/10.1016/j.cryogenics.2022.103588

Baiocco, P., & Bonnal, C. (2016). Technology demonstration for reusable launchers. *Acta Astronautica*, *120*, 43–58. https://doi.org/10.1016/j.actaastro.2015.11.032

Bhuva, V. J., Jani, J. P., Patel, A., & Tiwari, N. (2022). Effect of bubble coalescence on two-phase flow boiling heat transfer in raccoon microchannel - A numerical study. *International Journal of Heat and Mass Transfer*, *182*, 121943. https://doi.org/10.1016/j.ijheatmasstransfer.2021.121943

Brackbill, J. U., Kothe, D. B., & Zemach, C. (1992). A continuum method for modeling surface tension. *Journal of Computational Physics*, *100*(2), 335–354. https://doi.org/10.1016/0021-9991(92)90240-Y

Burkhardt, H., Sippel, M., Herbertz, A., & Klevanski, J. (2004). Kerosene vs methane: A propellant tradeoff for reusable liquid booster stages. *Journal of Spacecraft and Rockets*, *41*(5), 762–769. https://doi.org/10.2514/1.2672

Chen, J., Zeng, R., Chen, H., & Xie, J. (2020). Effects of wall superheat and mass flux on flow film boiling in cryogenic chilldown process. *AIP Advances*, *10*(1). https://doi.org/10.1063/1.5135643

Chen, J., Zeng, R., Zhang, X., Qiu, L., & Xie, J. (2018). Numerical modeling of flow film boiling in cryogenic chilldown process using the AIAD framework. *International Journal of Heat and Mass Transfer*, *124*, 269–278. https://doi.org/10.1016/j.ijheatmasstransfer.2018.03.087

Chuang, T. J., & Hibiki, T. (2015). *Vertical upward two-phase flow CFD using interfacial area transport equation.* Progress in Nuclear Energy (Vol. 85, pp.

415–427). Elsevier Ltd. https://doi.org/10.1016/j.pnucene.2015.07.008

Davanipour, M., Javanmardi, H., & Goodarzi, N. (2018). Chaotic self-tuning pid controller based on fuzzy wavelet neural network model. *Iranian Journal of Science and Technology - Transactions of Electrical Engineering*, *42*(3), 357–366. https://doi.org/10.1007/s40998-018-0069-1

Duan, Y., Pan, C., Wang, W., Li, L., & Zhou, Y. (2023). Design and optimization of heat exchanger in coaxial pulse tube cryocooler working above 100 K. *Cryogenics*, *129*(November 2022), 103607. https://doi.org/10.1016/j.cryogenics.2022.103607

Fang, X., Sudarchikov, A. M., Chen, Y., Dong, A., & Wang, R. (2016). Experimental investigation of saturated flow boiling heat transfer of nitrogen in a macro-tube. *International Journal of Heat and Mass Transfer*, *99*, 681–690. https://doi.org/10.1016/j.ijheatmasstransfer.2016.03.126

Ferrín, J. L., & Pérez-Pérez, L. J. (2020). Numerical simulation of natural convection and boil-off in a small size pressurized LNG storage tank. *Computers and Chemical Engineering*, *138*. https://doi.org/10.1016/j.compchemeng.2020.106840

Fertahi, S. ed-D., Bouhal, T., Agrouaz, Y., Kousksou, T., El Rhafiki, T., & Zeraouli, Y. (2018). Performance optimization of a two-phase closed thermosyphon through CFD numerical simulations. *Applied Thermal Engineering*, *128*, 551–563. https://doi.org/10.1016/j.applthermaleng.2017.09.049

Fu, X., Qi, S. L., Zhang, P., & Wang, R. Z. (2008). Visualization of flow boiling of liquid nitrogen in a vertical mini-tube. *International Journal of Multiphase Flow*, *34*(4), 333–351. https://doi.org/10.1016/j.ijmultiphaseflow.2007.10.014

Gao, Y., Wang, Z., Li, Y., Ma, E., & Yu, H. (2024). Flow boiling of liquid nitrogen in a horizontal macro-tube at low pressure: Part I - flow pattern, two-phase flow instability, and pressure drop. *International Journal of Heat and Fluid Flow*, *107*(January), 109335. https://doi.org/10.1016/j.ijheatfluidflow.2024.109335

Hartwig, J., Hu, H., Styborski, J., & Chung, J. N. (2015). Comparison of cryogenic flow boiling in liquid nitrogen and liquid hydrogen chilldown experiments. *International Journal of Heat and Mass Transfer*, *88*, 662–673. https://doi.org/10.1016/j.ijheatmasstransfer.2015.04.102

Hedayatpour, A., Antar, B. N., & Kawaji, M. (1993). Cool-down of a vertical line with liquid nitrogen. *Journal of Thermophysics and Heat Transfer*, *7*(3), 426–434. https://doi.org/10.2514/3.436

Heldens, J. C., Fridh, J., & Östlund, J. (2021). On the characterization of methane in rocket nozzle cooling channels. *Acta Astronautica*, *186*, 337–346. https://doi.org/10.1016/j.actaastro.2021.05.034

Hu, H., Chung, J. N., & Amber, S. H. (2012). An experimental study on flow patterns and heat transfer characteristics during cryogenic chilldown in a vertical pipe. *Cryogenics*, *52*(4–6), 268–277. https://doi.org/10.1016/j.cryogenics.2012.01.033

Iannetti, A., Girard, N., Tchou-kien, D., Bonhomme, C., Ravier, N., & Edeline, E. (2017). *Prometheus, a Lox/Lch4 Reusable Rocket Engine*. 7 Th European Conference for Aeronautics and Space Sciences (Eucass), 1–9. https://doi.org/10.13009/EUCASS2017-537

Jeon, G. M., Park, J. C., & Choi, S. (2021). Multiphase-thermal simulation on BOG/BOR estimation due to phase change in cryogenic liquid storage tanks. *Applied Thermal Engineering*, *184*(November 2020), 116264. https://doi.org/10.1016/j.applthermaleng.2020.116264

Jones, H. W. (2018, July). *The Recent Large Reduction in Space Launch Cost.* 48th International Conference on Environmental Systems, 81. https://ttu-ir.tdl.org/handle/2346/74082

Jouhara, H., Chauhan, A., Guichet, V., Delpech, B., Abdelkarem, M. A., Olabi, A. G., & Trembley, J. (2023). Low-temperature heat transfer mediums for cryogenic applications. *Journal of the Taiwan Institute of Chemical Engineers*, 104709. https://doi.org/10.1016/j.jtice.2023.104709

Kharangate, C. R., & Mudawar, I. (2017). Review of computational studies on boiling and condensation. *International Journal of Heat and Mass Transfer*, *108*, 1164–1196. https://doi.org/10.1016/j.ijheatmasstransfer.2016.12.065

Lee, J., Mudawar, I., Hasan, M. M., Nahra, H. K., & Mackey, J. R. (2022). Experimental and computational investigation of flow boiling in microgravity. *International Journal of Heat and Mass Transfer*, *183*, 122237. https://doi.org/10.1016/j.ijheatmasstransfer.2021.122237

Lee, W. H. (2013). *A Pressure iteration scheme for two-phase flow modeling.* Computational Methods For Two-Phase Flow And Particle Transport (Vol. 1, pp. 61–82). World Scientific. https://doi.org/10.1142/9789814460286_0004

Ling, T., Wang, T., Lei, G., Fang, Z., Zhao, L., & Xu, C. (2021). Experimental study on slug flow characteristics and its suppression by microbubbles in gas-liquid mixture pipeline. *Journal of Applied Fluid Mechanics*, *14*(2), 567–579. https://doi.org/10.47176/jafm.14.02.31482

Liu, Z., Li, Y., & Jin, Y. (2016). Pressurization performance and temperature stratification in cryogenic final stage propellant tank. *Applied Thermal Engineering*, *106*, 211–220. https://doi.org/10.1016/j.applthermaleng.2016.05.195

Meyer, M. L., Motil, S. M., Kortes, T. F., Taylor, W. J., &

Mcright, P. S. (2012). *cryogenic propellant storage and transfer technology demonstration for long duration in-space missions*. http://www.sti.nasa.gov

Rapp, D. (2016). *Human Missions to Mars*. Springer International Publishing. https://doi.org/10.1007/978-3-319-22249-3

Salerno, L. J., & Kittel, P. (1999). Cryogenics and the human exploration of Mars. *Cryogenics*, *39*(4), 381–388. https://doi.org/10.1016/S0011-2275(99)00043-0

Sha, W., Leng, G., Xu, R. S., & Li, S. (2024). Numerical simulationof inlet void fraction affecting oil-gas two-phase flow characteristics in 90° elbows. *Journal of Applied Fluid Mechanics*, *17*(7), 1524–1535. https://doi.org/10.47176/jafm.17.7.2341

Srinivasan, K., Seshagiri Rao, V., & Krishna Murthy, M. V. (1974). Analytical and experimental investigation on cool-down of short cryogenic transfer lines. *Cryogenics*, *14*(9), 489–494. https://doi.org/10.1016/0011-2275(74)90125-8

Sun, D., Qiao, X., Yang, D., & Shen, Q. (2023). Experimental study on a two-stage large cooling capacity stirling cryocooler working below 30 K. *Cryogenics*, *129*(November 2022), 103619. https://doi.org/10.1016/j.cryogenics.2022.103619

Wang, Y. Z., Hua, Y. X., & Meng, H. (2010). Numerical studies of supercritical turbulent convective heat transfer of cryogenic-propellant methane. *Journal of Thermophysics and Heat Transfer*, *24*(3), 490–500. https://doi.org/10.2514/1.46769

Linstrom, P. J., & Mallard, W. G. (2001). The NIST Chemistry WebBook: A Chemical Data Resource on the Internet. *Journal of Chemical & Engineering Data*, *46*(5), 10591063. https://doi.org/10.1021/je000236i

Wu, B., Firouzi, M., Mitchell, T., Rufford, T. E., Leonardi, C., & Towler, B. (2017). A critical review of flow maps for gas-liquid flows in vertical pipes and annuli. *Chemical Engineering Journal*, *326*, 350–377. https://doi.org/10.1016/j.cej.2017.05.135

Xie, H., Yu, L., Zhou, R., Qiu, L., & Zhang, X. (2017). Preliminary evaluation of cryogenic two-phase flow imaging using electrical capacitance tomography. *Cryogenics*, *86*, 97–105. https://doi.org/10.1016/j.cryogenics.2017.07.008

Yung, Y. L., Chen, P., Nealson, K., Atreya, S., Beckett, P., Blank, J. G., Ehlmann, B., Eiler, J., Etiope, G., Ferry, J. G., Forget, F., Gao, P., Hu, R., Kleinböhl, A., Klusman, R., Lefèvre, F., Miller, C., Mischna, M., Mumma, M., Newman, S., Oehler, D., Okumura, M., Oremland, R., Orphan, V., Popa, R., Russell, M., Shen, L., Sherwood Lollar, B., Staehle, R., Stamenković, V., Stolper, D., Templeton, A., Vandaele, A. C., Viscardy, S., Webster, C. R., Wennberg, P. O., Wong, M. L., Worden, J. (2018). Methane on mars and habitability: challenges and responses. *Astrobiology*, *18*(10), 1221-1242. https://doi.org/10.1089/ast.2018.1917

Zeghloul, A., & Al-Sarkhi, A. (2023). Improved Drift Flux Void Fraction Model for Horizontal Gas-liquid Intermittent Flow. *Journal of Applied Fluid Mechanics*, *16*(7), 1499–1510. https://doi.org/10.47176/jafm.16.07.1693

Zhang, H., Zhi, X., Gu, C., Qi, Y., & Qiu, L. (2022). Numerical analysis of cryogenic LOX-LN2 mass transfer characteristics under different textured surfaces. *Cryogenics*, 125. https://doi.org/10.1016/j.cryogenics.2022.103507

Zhang, Z., Jia, L., Dang, C., & Ding, Y. (2024). Experimental study on flow boiling characteristics of R134a inside high-heat-flux microchannels. *International Journal of Heat and Fluid Flow*, *107*(April), 109372. https://doi.org/10.1016/j.ijheatfluidflow.2024.109372

Zheng, Y., Chang, H., Chen, J., Chen, H., & Shu, S. (2019). Effect of microgravity on flow boiling heat transfer of liquid hydrogen in transportation pipes. *International Journal of Hydrogen Energy*, *44*(11), 5543–5550. https://doi.org/10.1016/j.ijhydene.2018.08.047